Monthly Notices of the ROYAL ASTRONOMICAL SOCIETY

MNRAS **533,** 1233–1250 (2024) https://doi.org/10.1093/mnras/stae1756
Advance Access publication 2024 July 22

Underluminous tidal disruption events

Pau Amaro Seoane[1,2,3]★

[1]*Universitat Politècnica de València, Cam Vera s/n, 46022, Spain*
[2]*Max-Planck-Institute for Extraterrestrial Physics, Garching, Germany*
[3]*Higgs Centre for Theoretical Physics, Edinburgh, UK*

Accepted 2024 July 8. Received 2024 June 21; in original form 2023 July 24

ABSTRACT

We have evidence of X-ray flares in several galaxies consistent with a star being tidally disrupted by a supermassive black hole (MBH). If the star starts on a nearly parabolic orbit relative to the MBH, one can derive that the fallback rate follows a $t^{-5/3}$ decay. Depending on the penetration factor, β, a star will be torn apart differently, and relativistic effects play a role. We have modified the standard version of the smoothed-particle hydrodynamics (SPH) code GADGET to include a relativistic treatment of the gravitational forces between the gas particles of a main-sequence (MS) star and a MBH. We include non-spinning post-Newtonian corrections to incorporate the periapsis shift and the spin-orbit coupling up to next-to-lowest order. We find that tidal disruptions around MBHs in the relativistic cases are underluminous for values starting at $\beta \gtrapprox 2.25$, i.e. the fallback curves produced in the relativistic cases are progressively lower compared to the Newtonian simulations as the penetration parameter increases. While the Newtonian cases display a total disruption, we find that all relativistic counterparts feature a survival core for penetration factors going to values as high as 12.05. We perform a additional dynamical numerical study that shows that the geodesics of the elements in the star converge at periapsis. We confirm these findings with an analytical study of the geodesic separation equation. The luminosity of TDEs must be lower than predicted theoretically due to the fact that the star will partially survive when relativistic effects are taken into account. A survival core should consistently emerge from any TDE with $\beta \gtrapprox 2.25$.

Key words: relativistic processes – quasars: supermassive black holes – transients: tidal disruption events.

1 MOTIVATION

A star passing very close to a massive black hole (MBH) may be torn apart because of the tidal effects, and the interaction of the stellar debris in the vicinity of the black hole will give rise to a burst of electromagnetic radiation. The characteristics of this tidal disruption event (TDE), such as its temperature, peak luminosity, and decay time-scale, are functions of the mass and spin of the central MBH. The subsequent accretion of the debris gas by the black hole produces additional emission, and leads to phases of bright accretion that may reveal the presence of a MBH in an otherwise quiescent galaxy (see, e.g. Wheeler 1971; Hills 1975; Frank & Rees 1976; Carter & Luminet 1982, 1983; Rees 1988a; Murphy, Cohn & Durisen 1991; Magorrian & Tremaine 1999; Syer & Ulmer 1999; Freitag & Benz 2002; Gezari et al. 2003; Wang & Merritt 2004), with rates that vary depending on various factors but are of the order of 10^{-5}–10^{-6} yr^{-1} (see e.g. Rees 1988b and Stone et al. 2020 for a recent review on the rates and characteristics). These phenomena can be used as a probe of accretion physics close to the event horizon (Brenneman 2013; Reynolds 2014).

Many disruption candidates have already been detected with *ROSAT*, *Chandra*, *Swift* (see e.g. https://tde.space), and the ZTF (van Velzen et al. 2020), and the number will surge with upcoming transient surveys like the Large Synoptic Survey Telescope (LSST), SRG/eROSITA (Khabibullin, Sazonov & Sunyaev 2014), as well as the ESA L2 mission Athena (Nandra et al. 2013).

A conondrum related to optically-discovered TDEs is that their colour temperatures are significantly below the values predicted by theoretical models (Gezari et al. 2012; Arcavi et al. 2014; Chornock et al. 2014; Holoien et al. 2014; van Velzen & Farrar 2014). Observations depict a temperature and bolometric luminosity well below theoretical predictions based on accretion, and based on the same model, the derived blackbody emission radius implies an orbital motion below the expected theoretical values. In general, the fallback model requires masses much less than a solar mass in order to explain the difference in luminosity between the observed flares and the theoretical expectations.

Different theoretical models have been put forward to explain this fact. The work of Li, Narayan & Menou (2002) suggested that the low luminosity may indicate that the disrupted star is a brown dwarf or a planet. An alternative explanation is that the assumption that the gas immediately circularizes when it comes back close to the MBH is not accurate, and could trigger internal shocks that would result in a reduced luminosity. In particular, Piran et al. (2015) suggested that the released energy via internal shocks is responsible for the observed optical TDE candidates. More recently, Zhou et al. (2020) argued that the disc does not circularize and remains eccentric, which, as a consequence, leads the orbital energy of the stellar debris to be advected onto the MBH without being radiated away.

★ E-mail: amaro@riseup.net

In this work, we show with a set of smoothed-particle hydrodynamics (SPH) simulations with relativistic corrections that unbound stars lead to partial disruptions, which naturally explain the difference in the observed luminosity, for penetration values as deep as $\beta = 12.05$.

2 RELATIVISTIC IMPLEMENTATION

Relativistic effects have been considered in the related literature by e.g. Tejeda et al. (2017), which implemented a relativistic description of the evolution of the hydrodynamical elements with a quasi-Newtonian treatment of the fluid's self-gravity.

Earlier this year, Ryu and collaborators presented a series of works that also addressed TDEs in a relativistic fashion. For this approach, they depart from the intrinsically conservative GR hydrodynamical numerical code of Noble, Krolik & Hawley (2009), designed to study magnetohydrodynamic (MHD) turbulence in accretion discs around MBHs. To study TDEs, they assume that space–time is Schwarzschild plus contributions from the star self-gravity, and the dynamics of the star is described by hydrodynamics, solving the general-relativistic energy-momentum equations in the Schwarzschild background. This, hence implies that in the absence of material forces, the fluid elements strictly follow geodesics. The self-gravity of the star is described in the weak field, taking into account only the Newtonian gravitational potential. They then evolve the hydrodynamical equations in a frame where the metric is nearly flat and move the whole system in a rigid way along the orbit using parallel transport of the local frame. Hence, it is the trajectory of the system that 'sees' the Schwarzschild metric but the fluid elements almost live in a flat space–time.

More precisely, they consider a modified metric, $\tilde{g}_{\mu\nu} = g_{\mu\nu} + h_{\mu\nu}$, with $g_{\mu\nu}$ the Schwarzchild metric and $h_{\mu\nu}$ accounts for the self-gravity of the star. They assume the self-gravity is weak, so that the only non-zero component of the self-gravity perturbations is the time–time one: $h_{\rm tt} = -2\Phi_{\rm sg}/c^2$, where $\Phi_{\rm sg}$ is the Newtonian potential of the star in the sense that it satisfies a Poisson equation, where the mass density is replaced by the star proper rest-mass density. The procedure to incorporate this self-gravity is a bit more intricate than adding it to the Schwarzschild metric. The assumptions made to compute the self-gravity contribution include that the metric of Schwarzschild should not deviate from the Minkowski metric. Here is where the intrincacy mentioned comes in, since they need a parallel-transported tetrad adapted to the star, as mentioned before, so that in that frame the assumptions made are valid. It is important to note that they separate the problem of solving the hydrodynamical equations from the motion of the star around the MBH. This can be envisaged as having a frame centre at the (centre of mass) star where the metric, in an orthonormal basis, is exactly Minkowski (deviating as we move from the centre of mass). Then they solve the hydrodynamical equations in this frame, and the motion of the star is 'rigid' (only the centre of mass moves) according to the parallel-transport equations for the orthonormal basis (see Ryu et al. 2020b). In their calculations, all stars have net bound orbits by an amount of the order $\sim 10^{-10}c^2$–$10^{-3}(\sigma^2/2)$, where σ is the bulge dispersion and c the speed of light.

With this scheme, they investigate TDEs in four additional works. In Ryu et al. (2020a), they find that the critical pericenter distance for full disruptions is enhanced by up to a factor of ~ 3 as compared to the Newtonian case, and that it depends on the mass of the star in a non-trivial way (see Guillochon & Ramirez-Ruiz 2013, for previous work). The results of Ryu et al. (2020c) regarding partial disruptions show that due to the little mass distributed at low energies, late-time fallback is suppressed. The mass return rate should then be $\propto t^{-p}$ with $p \in [2, 5]$ in partial disruptions. In Ryu et al. (2020d), they show that relativistic effects induce width delays in the debris energy so that the magnitude of the peak return rate decreases. These results had already been pointed out by the previous work of Ivanov & Chernyakova (2006), Kesden (2012), Servin & Kesden (2017), although Ryu and collaborators provided quantitative corrections to these previous treatments. In Krolik, Piran & Ryu (2020), they discuss the event rates and the fate of the rest of the star, which is not disrupted (i.e. the amount of mass still inside the computational box when they stopped the simulation), which might interact with the MBH on a second periapsis passage or rejoin the stellar cluster. As we will see, in this work we find a surviving core in all relativistic simulations, which is in contradiction with a total disruption.

In this work, we modify the acceleration computation of GADGET (Springel 2005) to include relativistic corrections, which are based on the post-Newtonian (PN) formalism for the interaction between two bodies (in our case, each of the hydrodynamical particles and the MBH). This means that we simply add relativistic correcting terms to the Newtonian gravitational forces calculated between the MBH and the hydrodynamical particles that form the star during the whole simulation, which initially is set on a completely unbound orbit. This approximation allows us to capture the relativistic effects while allowing us to study the evolution of the star to larger radii without any other approximation than those inherent to SPH methods and the post-Newtonian expansion, valid in this regime of low (but yet relativistic) velocities. In this regard, our scheme is self-consistent and all phenomena related to relativistic effects and hydrodynamics emerge naturally by integrating the system.

The relative acceleration, in the centre-of-mass form, i.e. following the scheme of Brem, Amaro-Seoane & Spurzem (2013a), including all PN corrections can be written in the following way:

$$\frac{\mathrm{d}\vec{v}}{\mathrm{d}t} = -\frac{Gm}{r^2}[(1+A)\vec{n} + B\vec{v}] + \vec{C}_{1.5,\rm SO}. \tag{1}$$

In this equation, $\vec{v} = \vec{v}_1 - \vec{v}_2$ is the relative velocity vector, $m = M_\bullet + m_{\rm gas}$, the total mass with $M_\bullet$, the mass of the MBH, and $m_{\rm gas}$ the mass of a gas particle, r the separation and $\vec{n} = \vec{r}/r$. A and B are coefficients that can be found in Blanchet & Iyer (2003). Since we are modelling extremely light gas particles around a MBH, we adopt the terms in the limit $m_{\rm gas} = 0$. We consider the leading order spin-orbit interaction, with the term $\vec{C}_{1.5,\rm SO}$, in which the subscript SO stands for spin-orbit coupling, which can be found in (Tagoshi, Ohashi & Owen 2001; Faye, Blanchet & Buonanno 2006), and the first post-Newtonian correction to periapsis shift. We do not include dissipative terms because, contrary to an extreme-mass ratio inspiral (Amaro-Seoane 2018), the star only has one periapsis passage, and the gravitational radiation can be neglected. All the PN interactions are only considered between a gas particle and the MBH and are evaluated at all times during the whole integration. In all simulations with spin, we set the dimensionless spin vector to $\vec{a} = (0.7, 0.7, 0)$, so we get maximum precession of the orbit of the star orbit lying in the X–Y plane.

The implementation of these relativistic terms follows the prescription given in the work of Kupi, Amaro-Seoane & Spurzem (2006), which was the first work published about the inclusion of post-Newtonian corrections in the context of stellar dynamics. The addition of the spin to the problem was presented, also for the first time, in a stellar-dynamics context in Brem, Amaro-Seoane & Spurzem (2013b). Both the periapsis shift and the spin terms have been tested in detail, and partially published in the work of Brem et al. (2013b), with a series of comparisons with the semi-Keplerian approximation of Peters (1964).

3 INITIAL CONDITIONS

In all simulations, the mass of the MBH is $m_\bullet = 10^6\,\mathrm{M}_\odot$, the mass of the star is $m_\star = 1\,\mathrm{M}_\odot$, and it is set on an unbound, parabolic trajectory around the MBH, placed at the focus. It must be noted that while bound orbits are less 'expensive' computationally, the most natural orbits are unbound ones, i.e. parabolic or hyperbolic, because we do not expect the region of phase-space close to the MBH to produce bound orbits, at least in a Milky Way-like galaxy (see, e.g. Amaro-Seoane 2018; Baumgardt, Amaro-Seoane & Schödel 2018; Gallego-Cano et al. 2018; Schödel et al. 2018).

When the stars approach the MBH, it will experience strong tidal forces whenever the work exerted over the star by the tidal force exceeds its own binding energy, (all energies are per unit mass), which is

$$E_{\mathrm{bind}} = \frac{3\,Gm_\star}{(5-n)r_\star}, \tag{2}$$

where n is the polytropic index (Chandrasekhar 1942), $m_\star$ the mass of the star. This allows us to introduce a typical radius for this to happen, the tidal radius r_t. Considering $r_\star \ll r_\mathrm{t}$,

$$r_\mathrm{t} = \left[\frac{(5-n)}{3}\frac{m_\bullet}{m_\star}\right]^{1/3} 2\,r_\star. \tag{3}$$

With $m_\bullet$ the mass of the MBH. For a solar-type star, considering an $n = 3$ polytrope, and $m_\bullet = 10^6\,\mathrm{M}_\odot$, we have that

$$r_\mathrm{t} = 110\,R_\odot \sim 0.51\,\mathrm{au}. \tag{4}$$

The initial distance of the star to the MBH is set to 20 times the axis of symmetry of the parabola, i.e. the pericentric distance between the MBH and the star. In order to investigate the fate of the bound material to the star and the fallback rate, we have chosen a series of trajectories with different penetration factors β, which is defined to be the ratio between the tidal radius and the distance of periapsis, 1.5, 2, 3, 4, 5, and 9, and run for each case (i) a Newtonian simulation, (ii) a relativistic simulation taking into account only the periapsis shift of the SPH particles, and (iii) a relativistic simulation taking into account this effect and the spin correction.

It must be noted that the value for the penetration factors has been estimated by assuming a point-particle trajectory. However, in the relativistic cases, an initially assigned value for β diverges as the star progresses in its orbit towards the MBH as a function of the penetration factor. When the extended star achieves the vertex of the parabola, the penetration factor has differed from the initially chosen value. Hence, we initially set the star in that point-particle trajectory for those specific β values, and we derive the real penetration factor when it reaches the verteces of the relativistic cases. These are $\beta = 1.64,\ 2.26,\ 3.62,\ 5.15,\ 6.83$, and 12.05, and we use them in the Newtonian cases as well so as to be able to compare the results. These values in turn correspond to the following distances of periapsis: $r_\mathrm{peri} \sim 0.32,\ 0.22,\ 0.14,\ 0.1,\ 0.07,\ 0.04$ au. For a parabolic orbit, the velocity of the star at periapsis is $v_\mathrm{peri} = \sqrt{2\,\mu/r_\mathrm{peri}}$, with $\mu = Gm_\bullet \simeq 1.3 \times 10^{26}\,\mathrm{m^3\,s^{-2}}$, so that the corresponding velocities are $v_\mathrm{peri} \sim 7.37 \times 10^7,\ 8.88 \times 10^7,\ 1.11 \times 10^8,\ 1.32 \times 10^8,\ 1.57 \times 10^8,\ 2.08 \times 10^8\,\mathrm{m\,s^{-1}}$, which in units of the speed of light c are, respectively, 0.24, 0.29, 0.37, 0.44, 0.52, 0.69. In Fig. 1, we show 12 different snapshots in the evolution of a representative case with relativistic corrections, $\beta = 12.05$. We have displayed in red the densest regions of the star.

The stars are modelled as main-sequence (MS) stars with a polytrope of index 3 constructed initially following the method of (Freitag & Benz 2005, in particular; see their online complements). We employ half a million particles to construct the polytrope, which is enough to solve the tidal disruption process. Increasing the number of particles by less than an order of magnitude (or a factor of 10) does not necessarily lead to a significant improvement of the simulation (see section 3 of Rasio 2000), as we show in Section 7.3, in particular of the stellar density and temperature profile. We adopt a fixed softening length for the gas particles of 0.01 $R_\odot$. Taking into account that the deepest penetration factor we have used is of 12.05, and that the tidal radius is of 110 $R_\odot$, as we can see in equation (4), this means that the closes periapsis distance is of $\sim$9.13 $R_\odot$; i.e. almost three orders of magnitude larger than our softening, so that the simulation is well resolved. The has smoothing is adaptive, whereby the number of neighbours with which each particle interacts is constant, and set to 50.

4 QUANTITATIVE ANALYSIS

One important aspect in the process is the evolution of the star after the first periapsis passage. To determine which part of the gas particles in the simulation is still bound or unbound to the star, we follow the following prescription (based on the work of Lai, Rasio & Shapiro 1993; Fulbright, Benz & Davies 1995): So as to decide whether a gas particle i is bound to the star, we calculate the specific energy of this particle relative to the star,

$$\epsilon_i = u_i + \frac{1}{2}v_\mathrm{rel}^2 - \sum_j \frac{Gm_j}{r_{ij}}, \tag{5}$$

where u_i and v_rel are, respectively, the internal energy and the relative velocity of gas particle i to the centre of mass velocity of all the gas particles belonging to the star. The potential part is summed up over all star particles j. If $\epsilon_i > 0$, the particle is considered unbound from the star, otherwise bound. In the first step of the iteration, all particles are assumed to be star particles. After evaluating equation (5), particles are reassigned to be either still part of the star or unbound. In the next step, the specific energy is evaluated with respect to the reduced fraction of star particles. We stop the iteration when reassignments to the unbound component cannot be made. After the iteration is complete, we check which part of the gas that is no longer gravitationally bound to the star is on Keplerian orbits around the MBH or completely unbound from the system. This part of the gas is then considered for the luminous fallback onto the MBH.

In Fig. 2, we show the fate of the material stripped (bound) from (to) the star for the different penetration factors mentioned before up to 3.62. The scaling of the first two panels in all these figures is the same in order to be able to compare better. In all figures, we also add a third panel showing the long-term evolution of the Newtonian cases. We can see from these figures that the amount of bound mass to the star, i.e. the survival star, is in all cases larger in the relativistic simulations than in the Newtonian counterparts. For the relativistic cases, about 0, 40, and 20 per cent of the star survives the disruption after one day for the first three values of $\beta = 1.64,\ 2.26$, and 3.62, while in the Newtonian simulations, this quantity is only about 50, 5, 2 per cent. These results are generally in agreement with the amount of mass of the survival core found in the work of Ryu et al. (2020c).

In Fig. 3, we depict the same as in Fig. 2 for the two most extreme penetration factors, $\beta = 5.15,\ 12.05$ (this last penetration factor, the star is still at a distance of two Schwarzschild radii from a Schwarzschild MBH of mass $10^6\,\mathrm{M}_\odot$). In this case, the amount of bound material to the star in the Newtonian case further decreases as compared to larger β values. It is about 1 and 0 per cent, respectively.

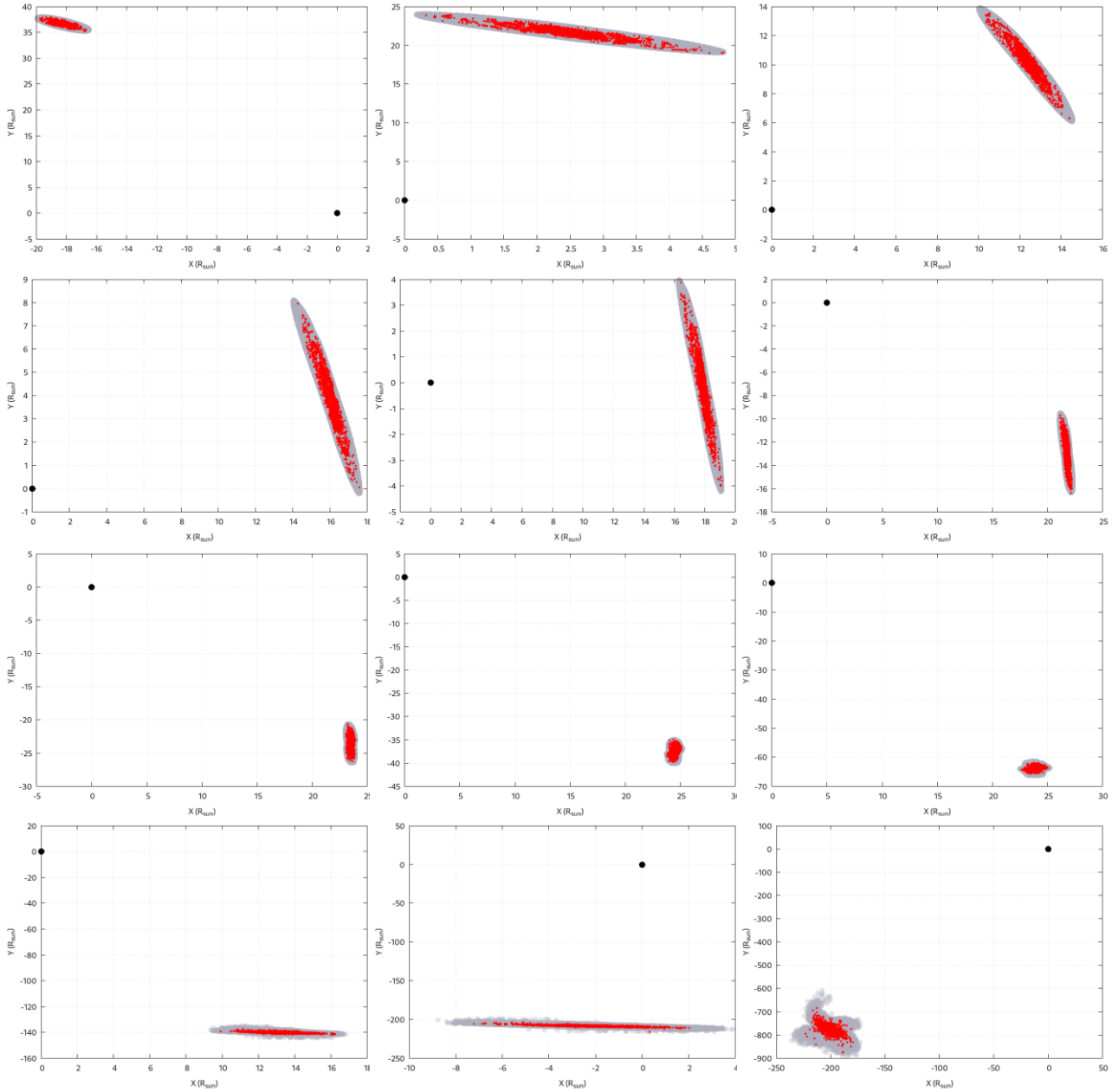

Figure 1. Tidal disruption of the $\beta = 12.05$ case with relativistic corrections. We can observe, from the top to the bottom, right to left, how the star becomes more elongated along its parabolic orbit around the MBH, represented with a black dot at the origin. After the stretching and compression of periapsis, the star recovers a somewhat spherical architecture to be stretched again. At much longer time-steps, which correspond to the last panel, the star is again more spherical, although with deformations. We do not show all the gas particles that we used in the simulation for clarity, and in red the densest regions in the star.

However, the relativistic cases show a much larger survival stellar object, with a mass of about 40 per cent. In the relativistic simulations, the amount of bound material to the star is larger than in their Newtonian counterparts, even at the smallest value of β.

In this first case, for $\beta = 1.64$, we observe in the Newtonian case of Fig.(2) that a significant amount of matter of the star survives the close interaction with the MBH. Indeed, Guillochon & Ramirez-Ruiz (2013) estimated that (Newtonian) TDEs have 100 per cent disruption only for penetration factors $\beta > 1.85$. Recently, Miles, Coughlin & Nixon (2020) have studied (Newtonian) partial disruptions that corroborate the fallback rate proportion of $\propto t^{-9/4}$. Other scenarios, like the progressive disruption of a star as result of a tidal separation, however, lead to different eccentricities that predict a different scaling of $\propto t^{-1.2}$ Amaro-Seoane, Miller & Kennedy (2012). Also, Ryu et al. (2020c) find $\propto t^{-p}$ with $p \in [2, 5]$ depending on the mass of the star and the role of their relativistic implementation.

In Fig. 4, we show the last snapshot of the Newtonian simulation with $\beta = 1.64$ using the visualization tool of Price (2007) to render the gas particles. Embedded in the figure, we have added a zoom of the area corresponding to what seems to be the remaining core of the star. However, this is a transient feature, as we can see in the uppermost, right-hand panel of Fig. 2. We integrated the system for

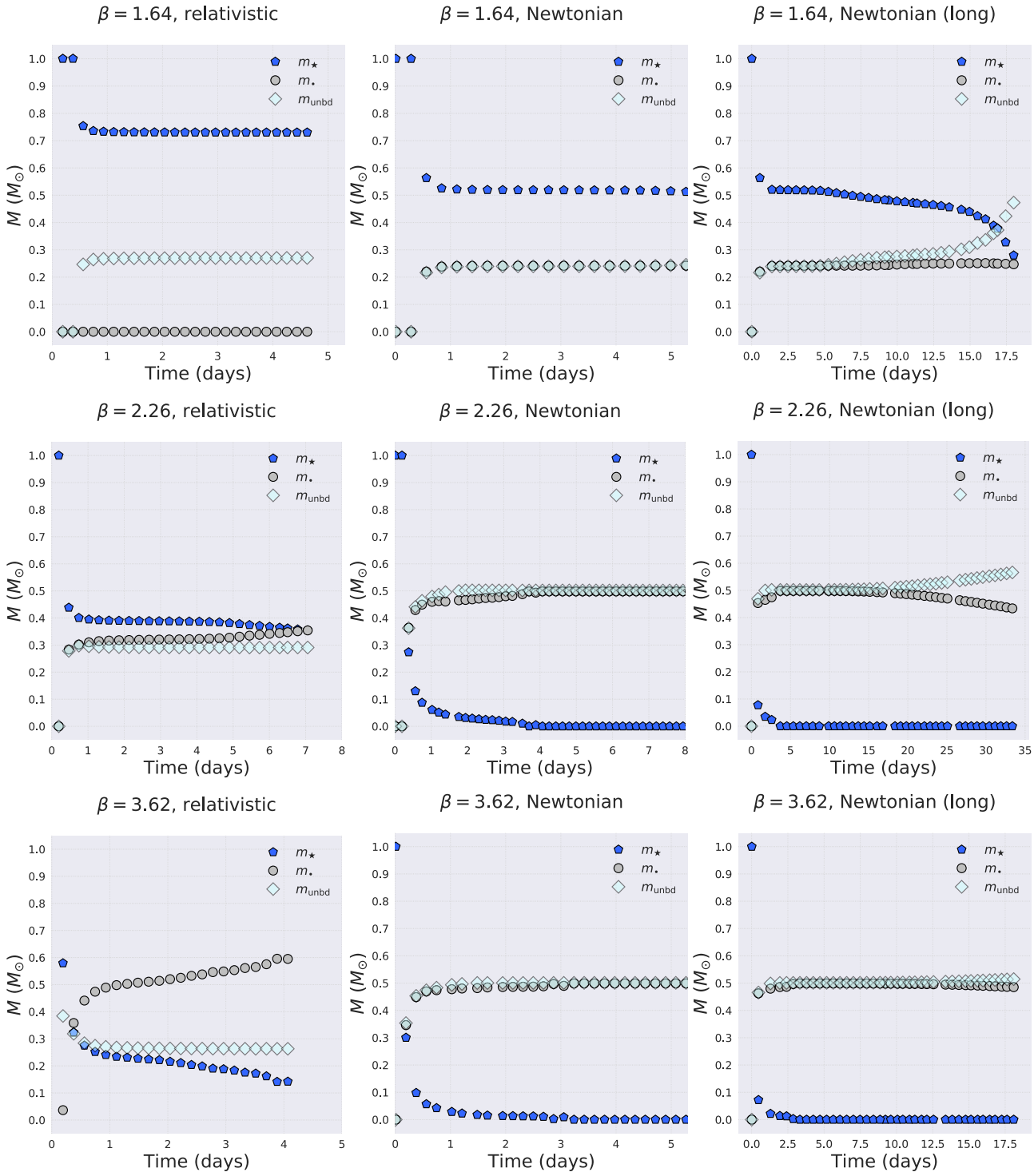

Figure 2. Amount of bound and ejected stellar mass for $\beta = 1.64$ as a function of time. In blue pentagons, we depict bound stellar mass to the star, i.e. this represents the evolution of how much of the star remains after the TDE. In grey circles, the amount bound to the MBH, and in cyan squares, the unbound stellar mass, i.e. the mass of the star that is ejected. The left-hand and middle panels correspond to the relativistic and Newtonian simulations set to the same limits, so as to be able to compare. The right-hand panel is the Newtonian case integrated significantly further than in the left panel (labelled 'long').

up to some ∼18 d from the starting point, and we can see that the amount of mass decays very quickly with time, while the amount of matter of the original star bound to the MBH is kept constant. This episodic core will not be bound to the star at later times. However, it appears later as an enhanced fallback of debris in the first panel of Fig. 5 at later times, as we will explain in the next section.

5 FALLBACK RATE

So as to test the implementation of the orbit and the behaviour of the SPH star, we calculate the fallback rate on to the MBH. For this, we calculate the required time for the bound debris to come back again to periapsis by estimating the specific energy of each particle,

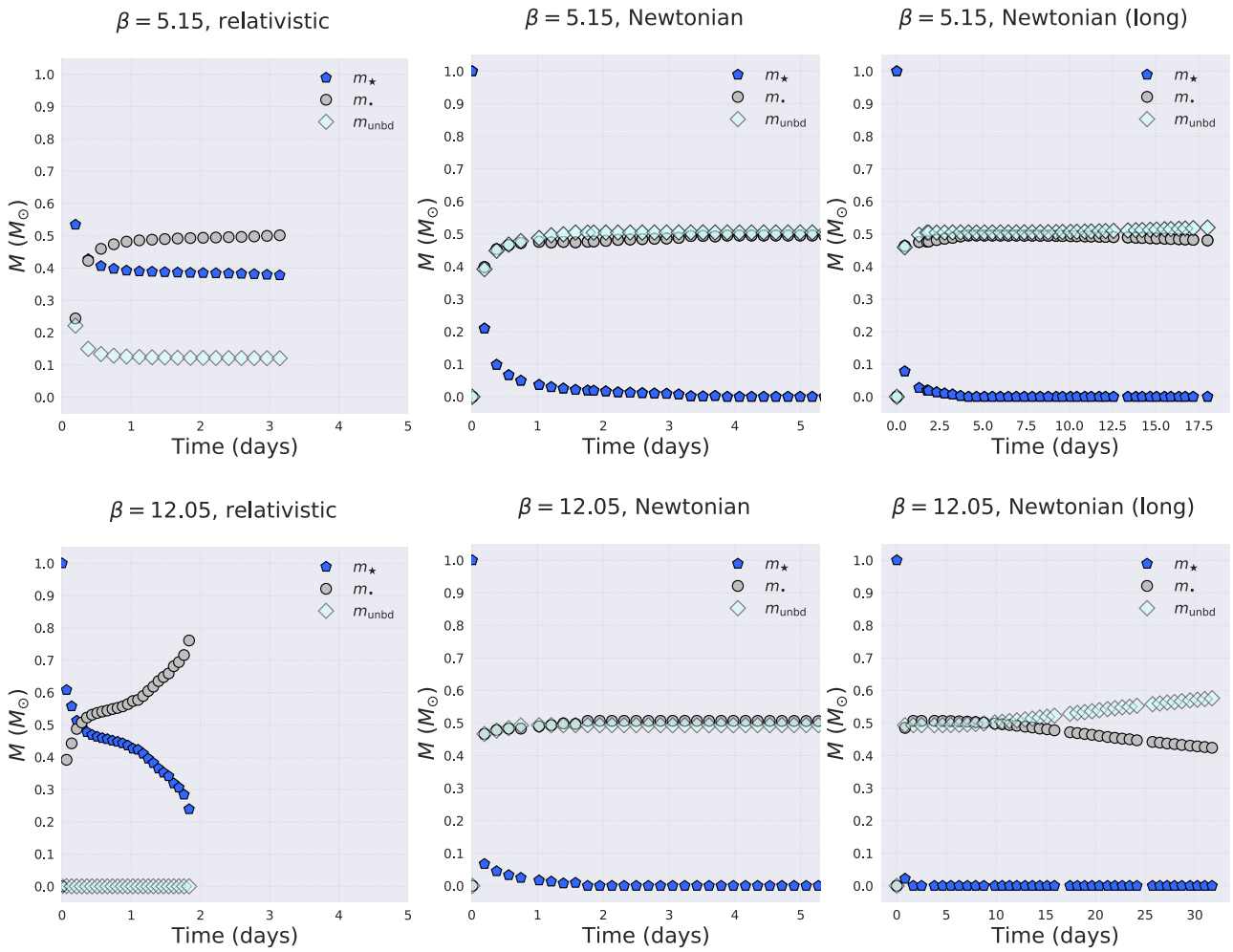

Figure 3. Same as Fig. 2 but for the two more extreme penetration factors, $\beta = 5.15$ and 12.05.

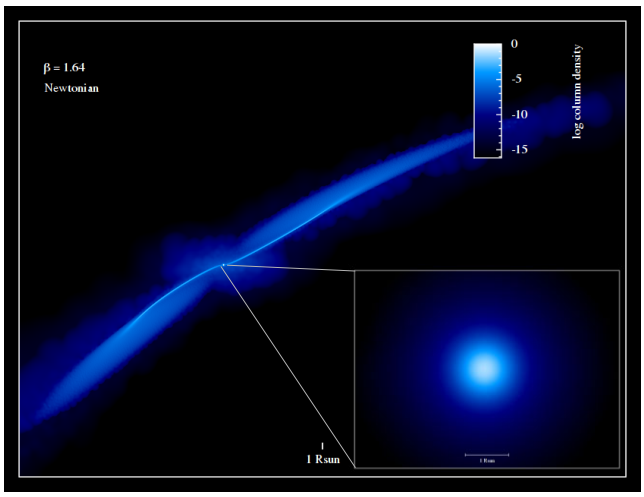

Figure 4. The last snapshot of the Newtonian simulation for $\beta = 1.64$. Both panels have a reference bar showing the length of a solar radius ('Rsun') to set the scale. The bar depicting the logarithm of the column density of gas in the zoom has been set to the minimum and maximum values of −3.43 and 0, respectively, for better identification of the structure.

$E = G\,(M + m)\,/(2\,a)$, with G the gravitational constant, M and m the masses of the MBH and one SPH particle, respectively.

From the angular momentum, one can derive that

$$e = \sqrt{1 + E\left(\frac{L}{\mu}\right)^2}, \tag{6}$$

where we have introduced $\mu = GM$ and neglect the contribution of m. If we define Δt as the ellapsed time between the first periapsis passage and the current position of the particle's position at a radius R from the MBH and time T, the necessary time for the next periapsis passage is $t_{\rm peri} = T - \Delta t$.

This distance is

$$R = a\ (1 - e \cdot \cos\epsilon)\,, \tag{7}$$

with ϵ the eccentric anomaly, so that $\epsilon < \pi$ for outbound motion and $\epsilon > \pi$ for inbound motion. The mean anomaly can be calculated as

$$M = 2\pi\delta t/T = \epsilon - e \cdot \sin\epsilon, \tag{8}$$

and allows us to calculate the ellapsed time since the last periapsis passage (at $M = 0$). We integrate the star's orbit until its centre of mass has travelled far away from the tidal radius out to $3000 R_\odot$, i.e. $\sim$12 730 $R_{\rm Schw}$, with $R_{\rm Schw}$ the Schwarzschild radius of the MBH. From this point on we assume, the gas particles to be travelling on

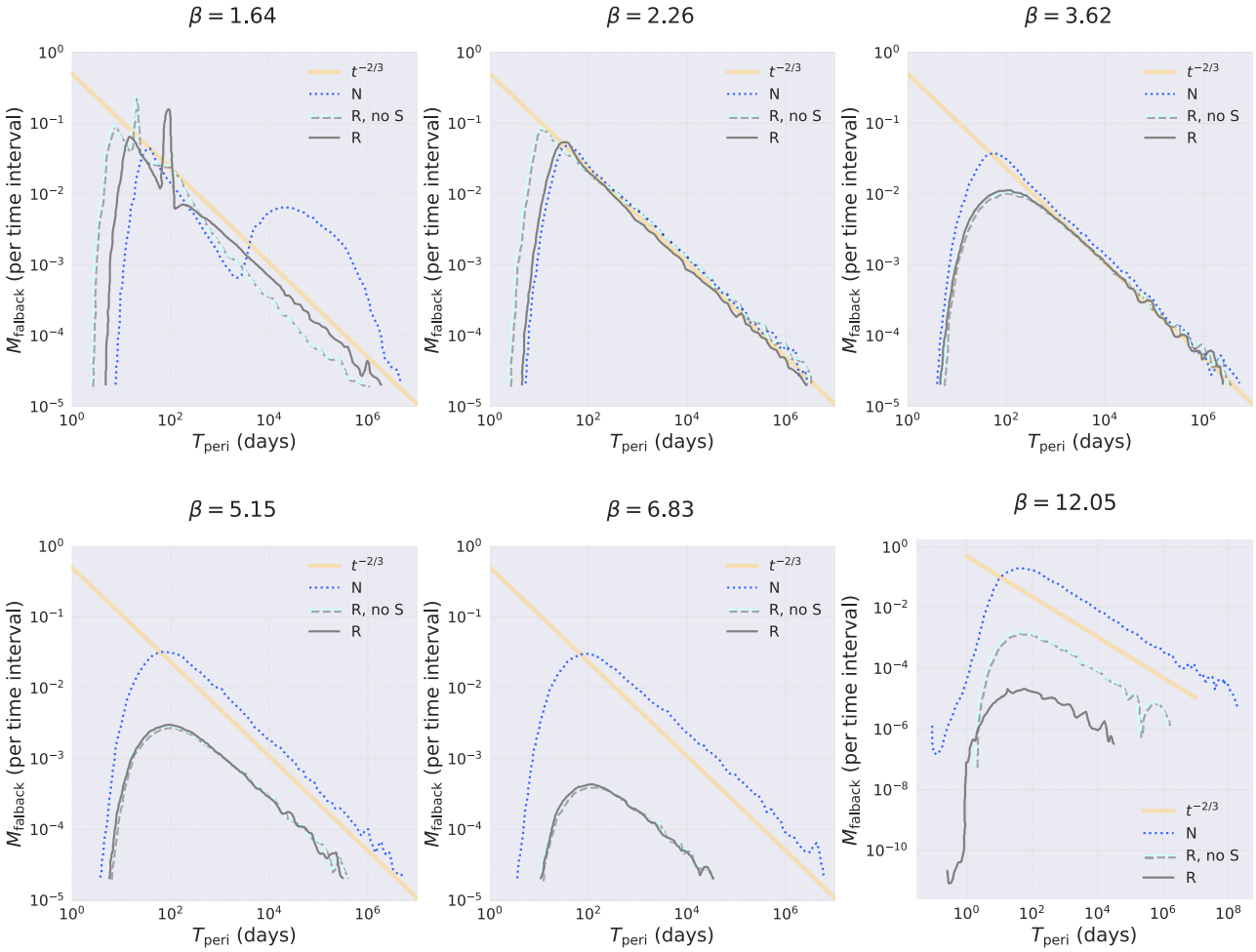

Figure 5. Fallback rate for a polytrope of index 3, mass 1 $M_\odot$, radius 1 $R_\odot$ and 500 000 particles. The curves delimit the upper part of histograms relative to the amount of bound stellar mass per time interval, distributed in intervals of $T_{\rm peri}$, in days. The dotted, blue curve corresponds to the Newtonian (N) simulations, the long-dashed, grey curves to the relativistic cases without spin (R, no S) and the solid, grey curves to the relativistic runs taking into account spin corrections (R). The solid, light-orange line depicts the power law described in the work of Rees in which the fallback rate is $\propto t^{-5/3}$. The reason for the exponent being $-2/3$ and not $-5/3$ is to correct for the logarithmic representation of the results, since the derivative of the mass M respect to the logarithm of time, t, $\mathrm{d}M/\mathrm{d}(\log(t)) \propto t \cdot \mathrm{d}M/\mathrm{d}t$. Hence, for a relation such as $\mathrm{d}M/\mathrm{d}t \propto t^{-x}$, $\mathrm{d}M/\mathrm{d}(\log(t)) \propto t^{-x+1}$, and so $-5/3 + 1 = -2/3$.

independent, non-interacting Keplerian orbits solely determined by their orbital energy and angular momentum. From these values we compute the classical time until the subsequent pericenter passage, $t_{\rm peri}$.

We present the results as fallback curves, which are mass histograms over $t_{\rm peri}$ in Fig. 5 for different values of the penetration factor β. We can see that the lower value of β leads to a drop in the Newtonian fallback between 10^2 and 10^4 d, which can be envisaged as a result of matter falling back more quickly. This forms the depression around the later enhanced fallback. This is matter that is bound to the MBH, not to the original star, which has started to become bound to itself after the evolution. The relativistic cases also display this feature, but at much earlier times and with much smaller depressions. This partial disruption leads to fallback values in the Newtonian case that are similar to the relativistic ones, as in the next value of $\beta = 2.26$. From that value upwards, the Newtonian cases lead to fallback values significantly higher than the relativistic ones, starting with about half an order of magnitude up to about five orders of magnitude for the deepest penetration and the spin case. We can observe only a clear effect of the spin when we go to extreme penetration values in the lowermost, right-hand panel, with $\beta = 12.05$.

In Fig. 6, we show a mosaic with nine different snapshots in the evolution of the Newtonian case of $\beta = 2.26$. As we zoom-in, we can see that at later times, 5.73 d, no surviving core is left. This situation changes completely when we consider the relativistic corrections, as we can see in its counterpart, Fig. 7, which takes into account the post-Newtonian correcting terms. We can clearly see the survival of a core that is bound to the original star, as shown in Fig. 2.

This difference becomes even more evident when comparing the extreme case of $\beta = 12.05$, in Fig. 8, the Newtonian case and Fig. 9. Short after the passage through periapsis, nothing is left from the original star in the Newtonian case, while in the relativistic one, we find a surviving core at much later times.

6 OPENING OF THE DEBRIS

In the simulations with a spin component, the debris opens and expands outside of the initial plan of the orbit. In Fig. 10, we display

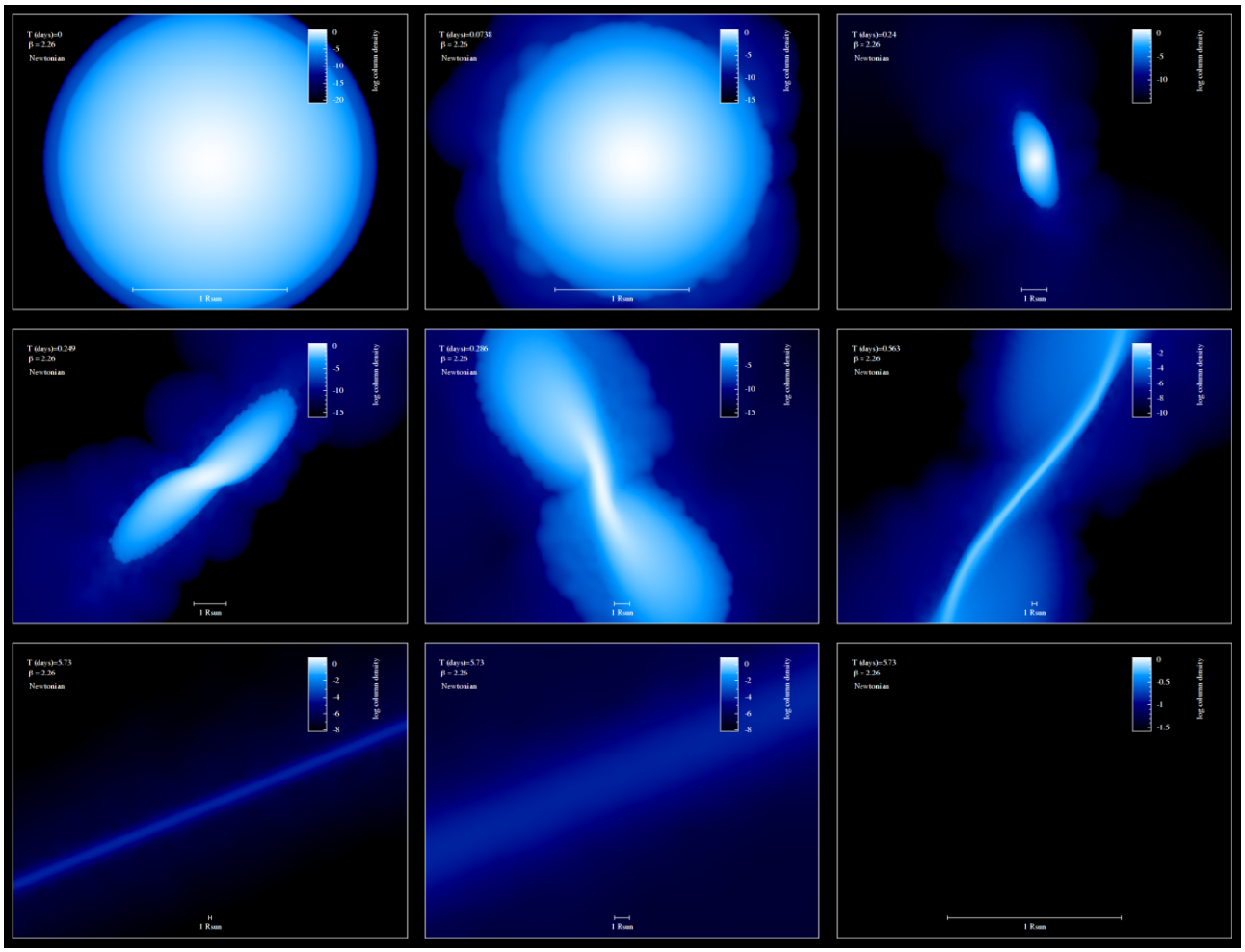

Figure 6. Mosaic of different instants of time corresponding to the Newtonian simulation of penetration factor $\beta = 2.26$. From the top to the bottom, left to right, we show six different moments in the evolution of the star in its reference frame, more specifically at (approximately) $T = 0$, 0.07, 0.24, 0.25, 0.29, 0.56, and 5.73 d. As a reference point, we show the length corresponding to one solar radius in each panel, and the (logarithm) of the column density of the star at the top on the right. Both the zoom factor and the depth of the logarithmic scale in the column density have been chosen in each frame to show the most interesting features, and they do not necessarily match from frame to frame. The last three panels depict the last moment, 5.73 d, at different zoom levels of the densest region. The last one shows an empty area because the depth of the column density is set to values not found.

this feature for one of the relativistic cases with spin. We show how the z-component of the angular momentum L_z normalized to the spin of the MBH evolves in time as compared to the x component, L_x, and we note that the results are similar for the y component. This outcome is particularly interesting because it could potentially lead to the intersection of the gas as it falls back onto the MBH with parts of the same debris, which are closer to the MBH. Such shocks can lead to afterglow flares, which are potentially observable.

However, one cannot solve this problem with an SPH-based code, since we cannot solve shocks. On the other hand, the amount of time needed for integration for the gas particles to achieve the maximum distance and fall back onto the MBH is too long. The accumulation of numerical errors and required integration time make the exercise pointless. This is indeed why we have integrated analytically the evolution of the gas particles in the first place, as we explained before. One could come up with the idea of converting these particles again into blobs of gas after the analytical integration, but then the question remains open as to what thermodynamics those clumps of gas should follow. It would be wrong to assume that their thermodynamical equation of state is the same as it was when the star underwent the tidal disruption. For all of these reasons, we just indicate here that the gas does spread out after the disruption, but we do not make any attempt at trying to continue the simulation to follow any potential interesting electromagnetic emission.

7 PROPERTIES OF THE SURVIVING CORE

In this section, we evaluate the properties of the core in the Newtonian and relativistic case for the most extreme case we have studied, $\beta = 12.05$. In Figs 11 and 12, we show the projection in the X- and Y-plane of the column density for both the Newtonian and relativistic cases at approximately the same time. As in the previous sections, we can observe a peak of density in the relativistic case, pinpointing the location of the surviving core. It is also interesting to observe that the relativistic case has a more complex structure than the Newtonian one, due to the twisting of the spin acting on the internal structure of the star.

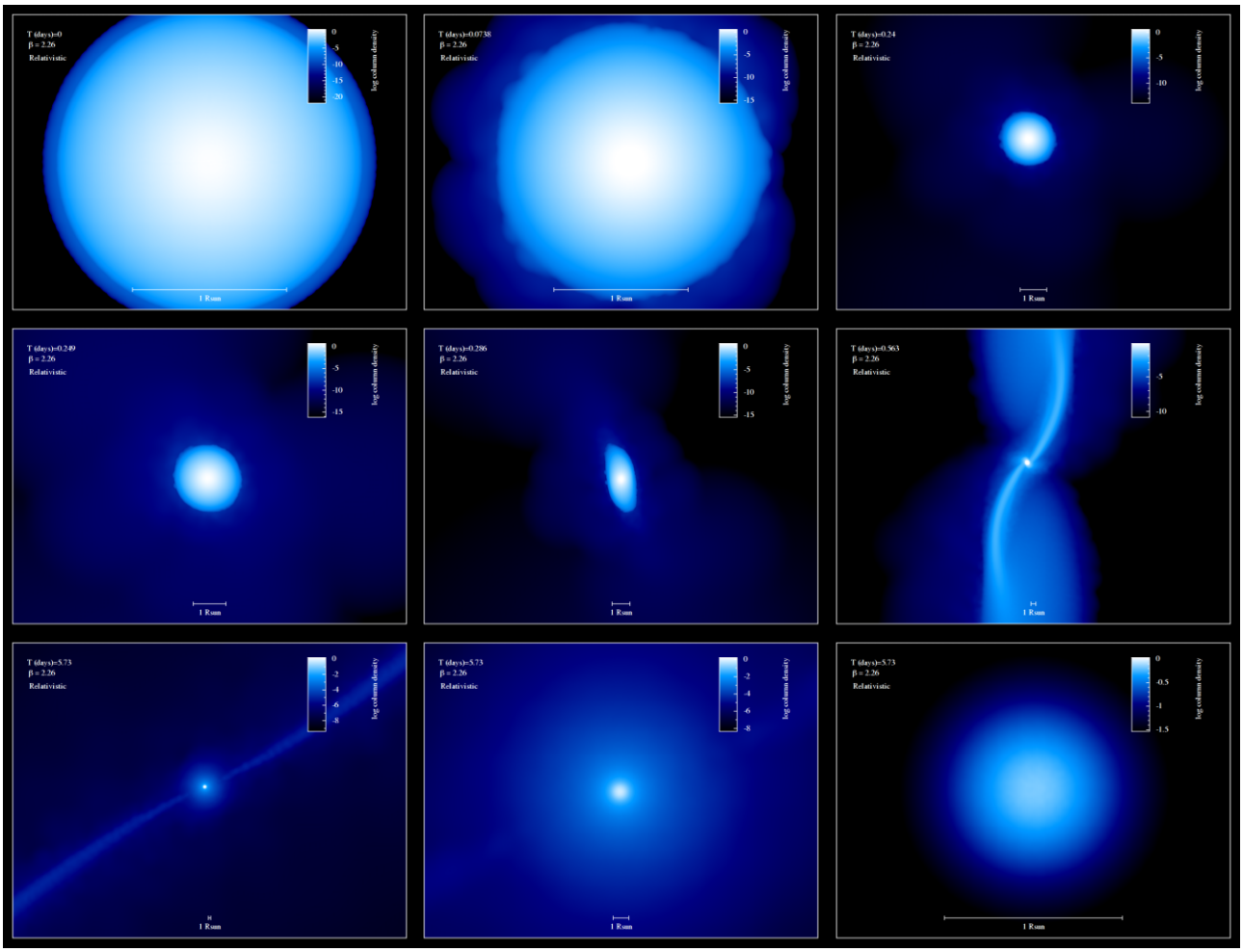

Figure 7. Same as Fig. 6 for the relativistic counterpart. While in the previous figure, the last panels show a thread-like distribution of the gas debris, in the relativistic counterpart, we see a survival core with a size of about half of the initial star. Both, the lengths and the density of the gas have been set to almost identical values to those shown in Fig. 6, so as to be able to compare panel by panel of both figures.

7.1 An extreme case

In order to understand how much the orientation and magnitude of the spin affect the general results, we address the evolution of a star, which is tidally disrupted in the deepest penetration factor, $\beta = 12.05$, that we have considered so far for a particular configuration, in which the massive black hole has a spin value of 1 in the z-direction. In Fig. 13, we zoom-in from the largest possible picture to the size of the core. As in all previous relativistic cases, we see that the general results remain the same.

Although the structure of the star may appear to be, and is, in fact, different, it is dangerous to try to overinterpret the consequences and implications of this fact. We should remember that we are using an SPH method that, by construction, cannot or does not properly resolve shocks in the system under study. On the other hand, even if we were to study the evolution of the system over very long periods of time to see if the debris intersects, it would be difficult to understand how to translate that fact into observables, since we would have accumulated a non-negligible numerical error. The alternative of analytically integrating the ballistic trajectories of the gas particles to later re-form hydrodynamic structures is unrealistic, as mentioned before, since we would have no information on the thermodynamic properties that these structures should have once the gas particles agglomerate.

7.2 Fate of the core

Indeed, for the above reasons in Section 7.1, although it is interesting to understand the subsequent evolution of the core, in particular to see if it remains bound to the MBH, so that it returns to the pericentre of the orbit to undergo further disruptions, it does not make sense to do so numerically. Therefore, we integrate the system until a reasonable time, i.e. until the core of the star is at such a distance from the MBH that any relativistic effect is clearly negligible. Typically, this distance is at least a thousand solar radii. At this point, we calculate the centre of mass of the core to determine its coordinates and velocities, as well as its mass. Assuming that the core follows a Keplerian orbit, we integrate its evolution to determine how long it will take to reach both the apocentre of the orbit and the pericentre. In the case that the core is bound and returns to the MBH, we would have to investigate the role played by the dissipative terms of the post-Newtonian approximation. However, in all the cases we have presented in this paper, the core resulting from the TDE is not bound to the MBH, so that the possibility of successive TDEs is ruled out. How this depends on the initial conditions and the limitations of the numerical method we have used needs to be investigated in detail. However, all this would result in much more dense work than what we are already presenting and will be investigated elsewhere.

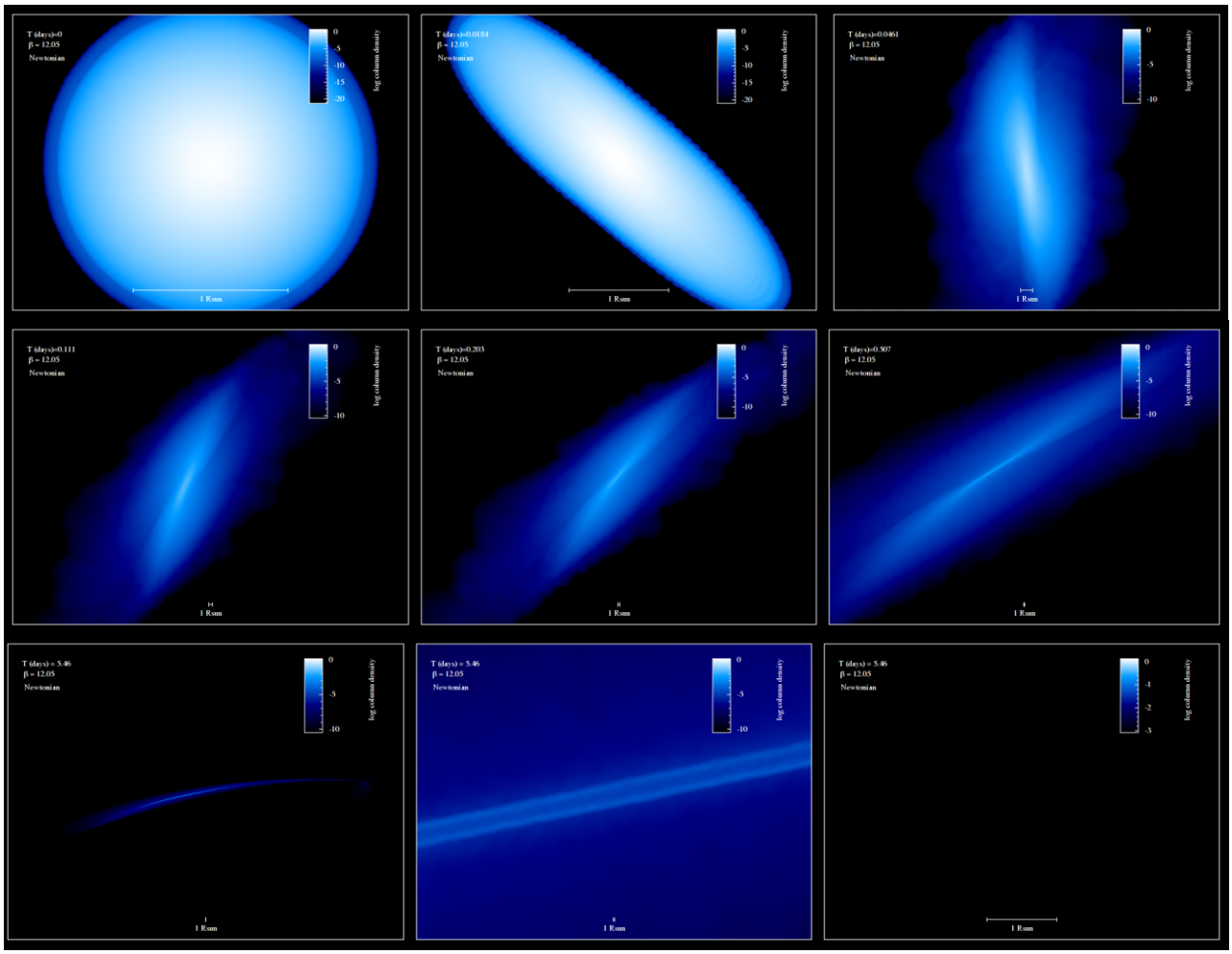

Figure 8. Same as in Fig. 6 but for a value of $\beta = 12.05$ and different times of the total integration. The last panel again shows nothing because the scale of the column density of the star is set to the same values as in Fig. 9, which we have chosen to show the survival core of the star. In this Newtonian case, however, the gas density is so low that nothing appears.

7.3 The role of the number of particles in the hydrodynamical simulations

So as to see whether the number of particles we have used previously is enough to capture the physics of the problem, we have performed an additional simulation with a total of 2×10^6 particles. Going beyond this number led to memory problems in the computer that we used to create the initial conditions. In Fig. 14, we show the usual density projection of the gas debris and surviving stellar core. In Fig. 15, we depict the density as a function of the three different axes. When comparing these results to their lower-resolution counterparts, i.e. Figs 9 and 12, we can see that the results we derived previously hold.

8 DISTANCE BETWEEN GEODESICS OF PARTICLES ON A PARABOLIC ORBIT AROUND A SPINNING MASSIVE BLACK HOLE

8.1 Numerical study

One better way to try to understand why a core survives in relativistic simulations is to calculate the geodesic convergence (or divergence) of the elements of the star as it approaches the pericentre of the MBH. The idea is to investigate if, in the relativistic case, the particles, which are to be envisaged as representative parts of the star, will come closer or not in the relativistic case as compared to the Newtonian one. In order to do so, we simulate the trajectory of six test particles using the numerical programme ARChain (Mikkola & Merritt 2006, 2008). This programme does not take into account hydrodynamics but pure, point-like dynamics. The advantage is that it is very accurate and features the implementation of the post-Newtonian terms as first presented in Kupi et al. (2006), which is the same we have used in the hydrodynamical experiments.

In Fig. 16, we show the Newtonian and relativistic cases without spin for six test particles on an initially parabolic orbit around a MBH. I.e. we want to see whether the particles tend to get closer in the relativistic case of this 'dust star' as compared to the Newtonian case. As we can see in the figure, in the Newtonian case, the particles follow the usual Keplerian trajectory (modulo some fluctuations due to their mutual attraction). The relativistic case undergoes precession, and the particles follow ballistic trajectories after the periapsis passage. That ulterior evolution is not representative of what different parts in a star would do, since, as explained, we are not taking into account hydrodynamics. The time-scale for the star to readjust to a perturbation caused by the gravitational interaction with the black hole is determined by the star's sound-crossing time, which is the

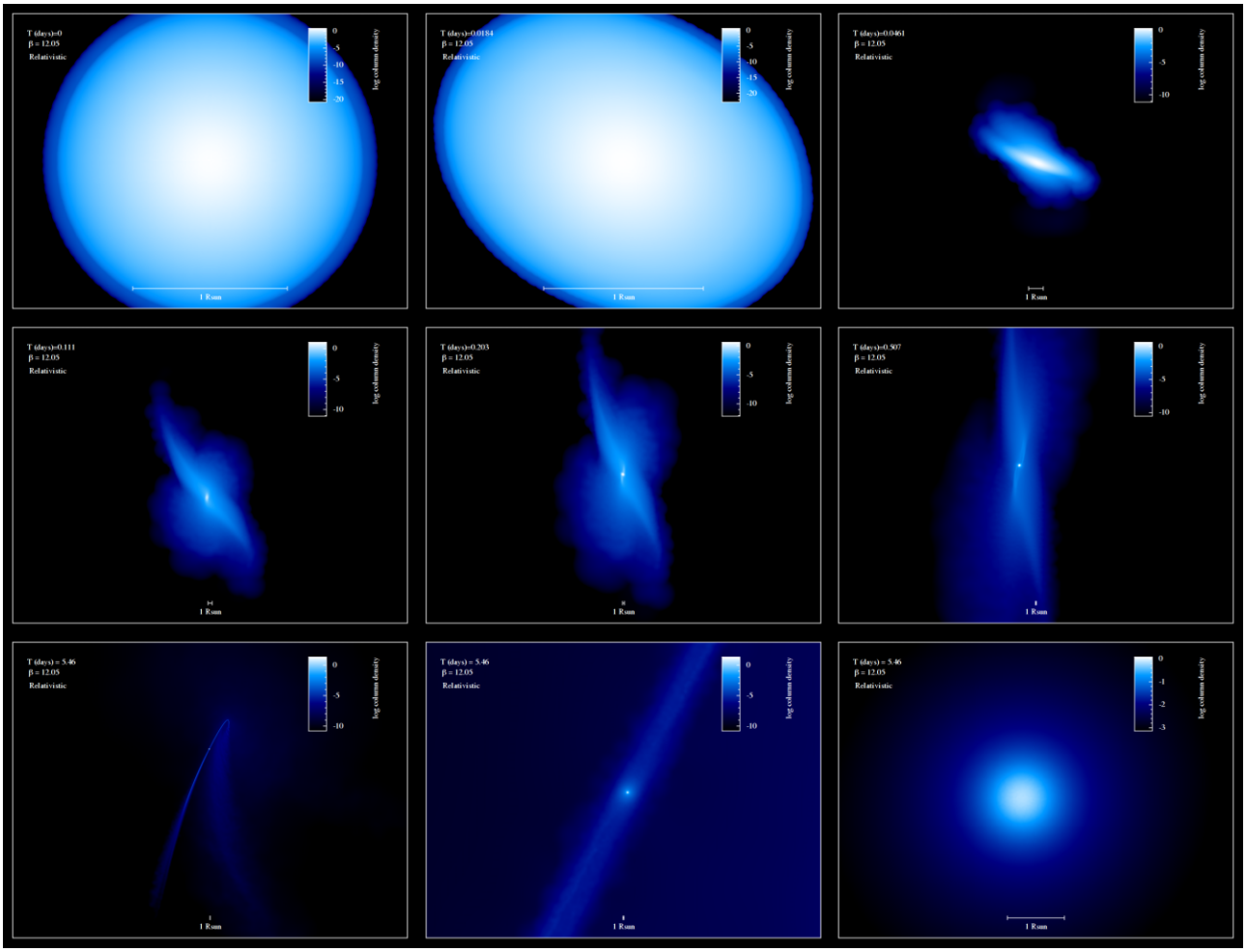

Figure 9. Same as Fig. 8 for the relativistic counterpart. Already in early times, the star in relativistic cases suffers a less significant spread in size. Also in this case, a survival core is found clearly in the simulation.

time it takes for a sound wave to travel across the star's diameter. For a typical main-sequence star with a radius of $R_\odot \approx 6.96 \times 10^8$ m and a sound speed of $c_s \approx 10^5\,\mathrm{m\,s^{-1}}$, the sound-crossing time is on the order of a few minutes. In the dynamical simulations, the time for a particle to go though the periapsis distance is smaller.

In Fig. 17 we show a similar comparison but for a relativistic case which takes into account the spin.

It is important to note that for this comparison to make sense, we need to focus at what happens at periapsis and not much farther beyond that point. However, the time-scale that dominates at periapsis is the relativistic one, so we can neglect hydrodynamics and assume point particles interacting only via gravity.

In Fig. 18, we depict the difference between the orbits in a two-particle case. We include two different relativistic treatments: one that does not take into account the spin of the MBH and another that does. As we can see, in the second case, the difference is the largest, meaning that the particles are getting a factor two of compression in the relativistic case when compared to the Newtonian one. Beyond the periapsis, the three different cases have very different evolutions because, as previously explained, we are in a purely dynamical regime; i.e. we do not take into account the hydrodynamics. It is interesting to see how the peaks in the difference of the relativistic cases are shifted as compared to the Newtonian one, since a smaller pericentre distance leads to a larger velocity and hence a shorter amount of time spent in that region.

The purpose of these dynamical test particle simulations is to illustrate why, in the relativistic case, particularly if we have spin, the star has a surviving core. As the star passes through periapsis, it will undergo an internal compression that will increase the density of the star, particularly at its centre. This result does not prove, but suggests that relativistic effects could indeed compress the star enough to allow some of it to survive the tidal stresses as a self-gravitating object. This is what we observe in Figs 2 and 3.

8.2 Analytical study

Now that we have seen that the dynamical study of the dust star leads to smaller distances at periapsis, confirming the results of the hydrodynamical simulations, what remains is to understand why this is the case, i.e. what is the physical reason for it. For this, let us consider the equation of geodesic deviation in proper time,

$$\frac{D^2\xi^{\mathrm{r}}}{\mathrm{d}\tau^2} = \left[R^{\mathrm{r}}_{\mathrm{ttr}}\left(\frac{\mathrm{d}t}{\mathrm{d}\tau}\right)^2 + R^{\mathrm{r}}_{\theta\theta r}\left(\frac{\mathrm{d}\theta}{\mathrm{d}\tau}\right)^2 + R^{\mathrm{r}}_{\phi\phi r}\left(\frac{\mathrm{d}\phi}{\mathrm{d}\tau}\right)^2\right]\xi^{\mathrm{r}}, \qquad (9)$$

where

$$\frac{D}{\mathrm{d}\tau} = \nabla_{\mathbf{u}} = u^\mu \nabla_\mu \qquad (10)$$

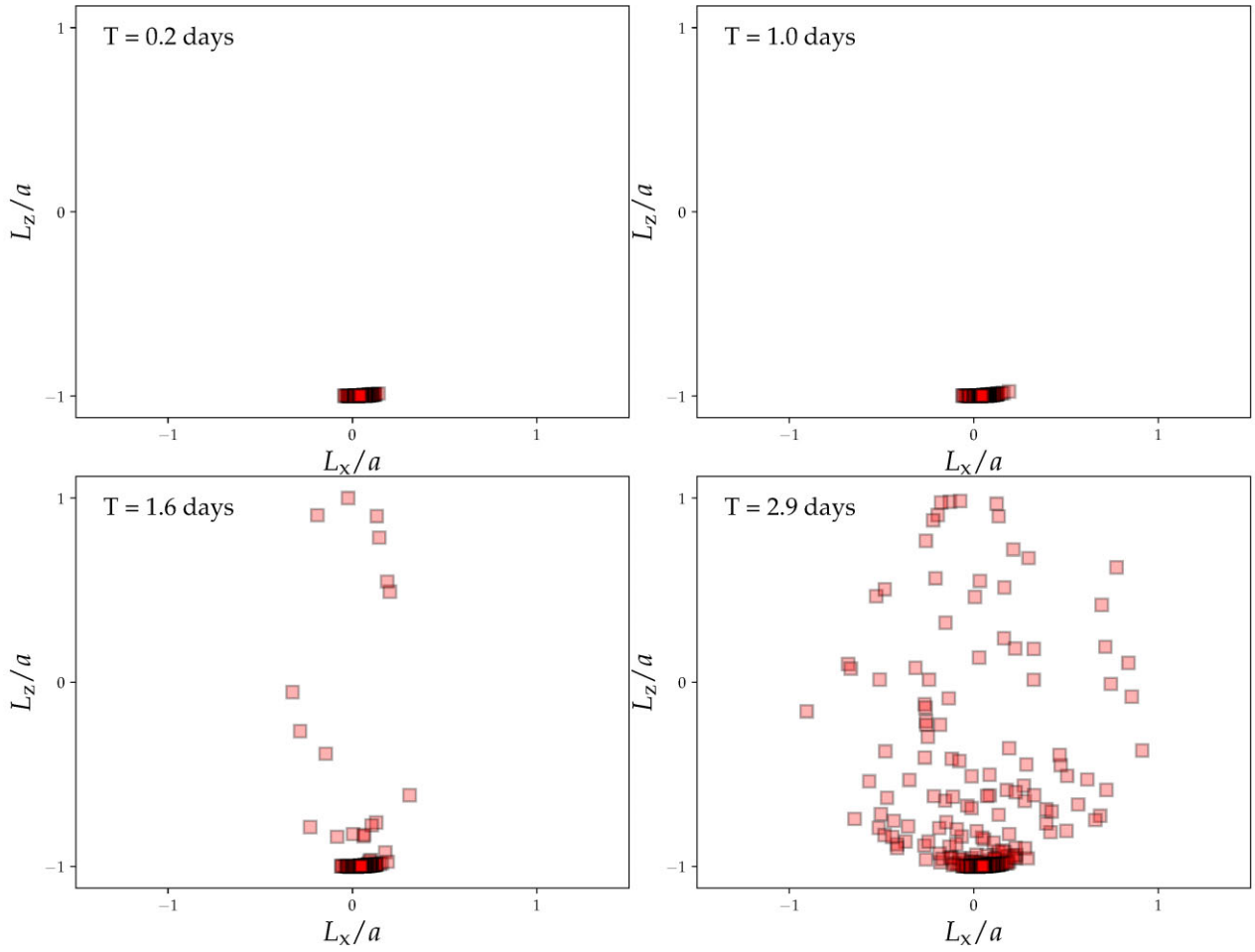

Figure 10. Components z and x of the angular momentum of the gas particles normalised to the spin of the MBH after the star has passed through periapsis. From the top to the right, we can see the evolution of the debris as a function of time in days.

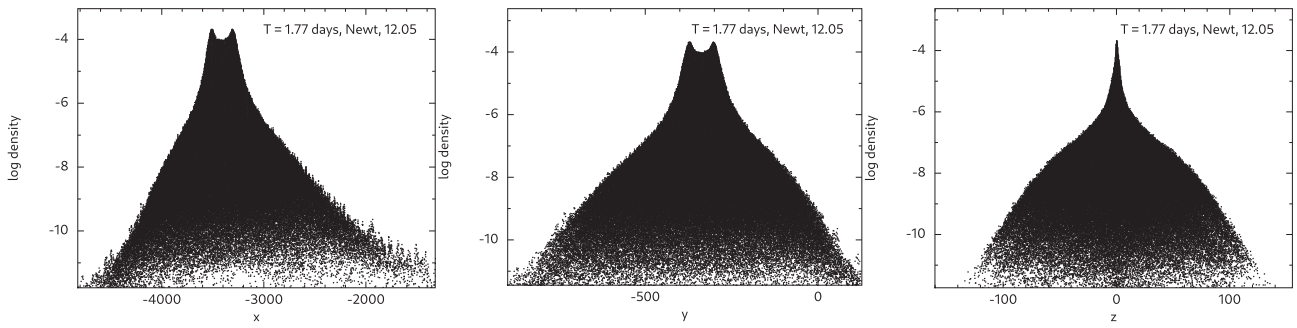

Figure 11. Projection of the density of the gaseous debris in the X-, Y-, and Z axis for $\beta = 12.05$ in the Newtonian case after 1.77 d.

is the covariant derivative along the observer's four-velocity; and

$$R^{\rm r}_{{\rm ttr}} = \frac{2Gm_\bullet}{r^3}\left(1-\frac{2Gm_\bullet}{rc^2}\right)$$
$$R^{\rm r}_{\theta\theta r} = \frac{Gm_\bullet}{rc^2}$$
$$R^{\rm r}_{\phi\phi r} = \frac{Gm_\bullet}{rc^2}\sin^2\theta, \qquad (11)$$

see e.g. Chandrasekhar (1998), and we have replaced the Schwarzschild radius with

$$R_{\rm Schw} = 2\frac{Gm_\bullet}{c^2}. \qquad (12)$$

It is important to note that, since we are neglecting the role of hydrodynamics and self-gravity, the test particles that conform to the dust star strictly follow geodesics. We consider a co-moving observer along these geodesics (i.e. an observer in the Fermi or free-fall coordinates), located on one of the test particles, who observes a locally flat space–time. Thus,

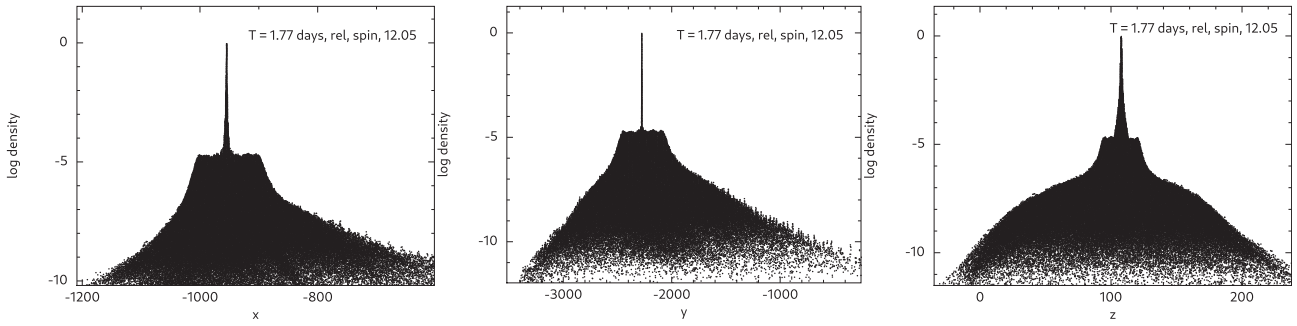

Figure 12. Same as Fig. 11 bur for the relativistic case. The spike corresponds to the surviving core.

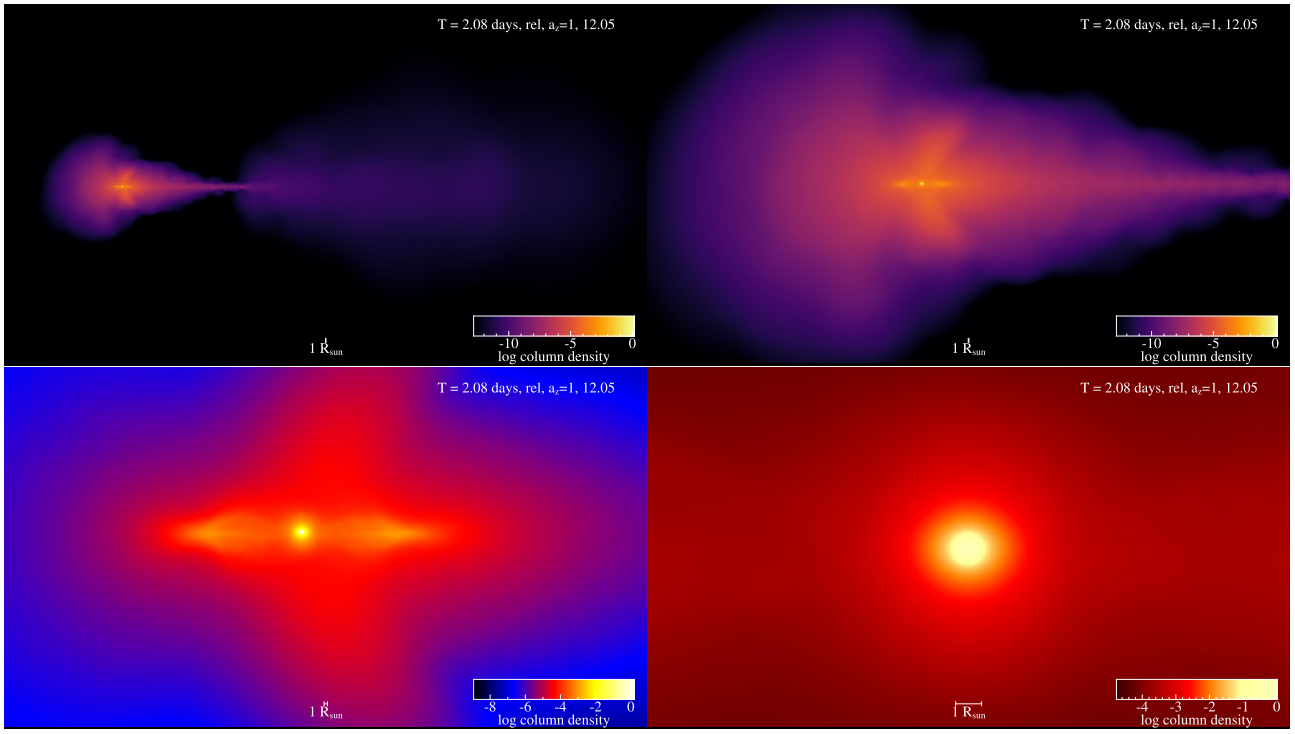

Figure 13. Density of the gaseous debris and surviving stellar core for the case in which the massive black hole is maximally spinning around the z-axis, in the relativistic case, after 2.08 d, for $\beta = 12.05$. From the top to the right, we show a progressive zoom-in of the projection to visualize the surviving core, which, as in the previous cases, has a size of about half a solar radius. Note that the column density ranges from different values as we zoom in, so as to define a more clear depiction of the gaseous particles in each panel.

$$\frac{\mathrm{d}t}{\mathrm{d}\tau} = c^2 \tag{13}$$

$$\frac{\mathrm{d}x^i}{\mathrm{d}\tau} = 0 \quad \text{for any spatial coordinate,} \tag{14}$$

and hence

$$\frac{D^2}{\mathrm{d}\tau^2} = \frac{\mathrm{d}^2}{\mathrm{d}t^2} + \frac{2Gm_\bullet}{r^2}\left(1 - \frac{2Gm_\bullet}{c^2 r^2}\right)^{-1}\frac{\mathrm{d}}{\mathrm{d}t} + \left(\frac{2Gm_\bullet}{r^2}\right)^2. \tag{15}$$

As a result, the geodesic deviation equation becomes

$$\frac{\mathrm{d}^2\xi^{\mathrm{r}}}{\mathrm{d}t^2} + \frac{2Gm_\bullet}{r^2}\left(1 - \frac{2Gm_\bullet}{rc^2}\right)^{-1}\frac{\mathrm{d}\xi^{\mathrm{r}}}{\mathrm{d}t} + \left[\left(\frac{2Gm_\bullet}{r^2c^2}\right)^2 - \frac{2Gm_\bullet}{r^3}\left(1 - \frac{2Gm_\bullet}{rc^2}\right)\right]\xi^{\mathrm{r}} = 0, \tag{16}$$

which is a second-order linear, homogeneous differential equation. Such an equation admits the general solution of the following type

$$\xi^r = C_1 \mathrm{e}^{\lambda_1 t} + C_2 \mathrm{e}^{\lambda_2 t}, \tag{17}$$

with C_1 and C_2 being two constants that are a result of the initial conditions and λ_1 and λ_2 two exponents that must fulfil

$$\lambda^2 + \frac{2Gm_\bullet}{r^2}\left(1 - \frac{2Gm_\bullet}{rc^2}\right)^{-1}\lambda + \left[\left(\frac{2Gm_\bullet}{r^2c^2}\right)^2 - \frac{2Gm_\bullet}{r^3}\left(1 - \frac{2Gm_\bullet}{rc^2}\right)\right] = 0. \tag{18}$$

This leads to the solutions

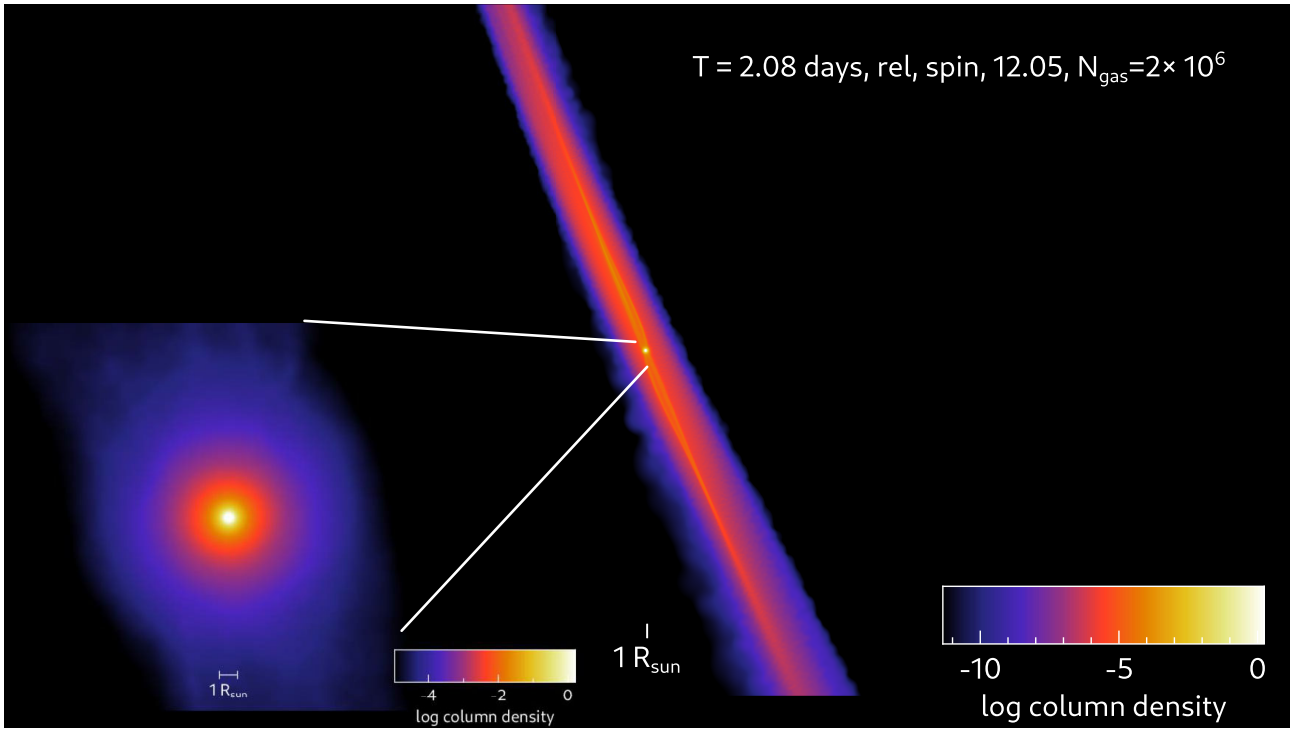

Figure 14. Same as Fig. 9 but for 2×10^6 gas particles.

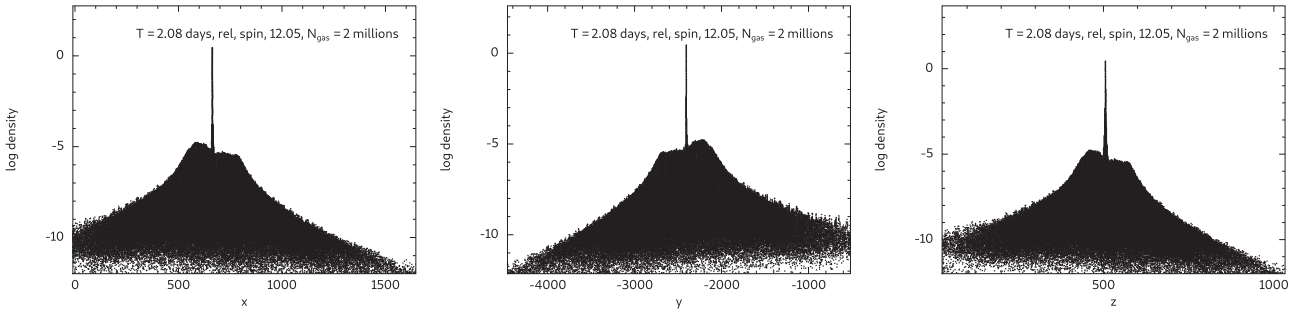

Figure 15. Same as Fig. 12 but for 2×10^6 gas particles.

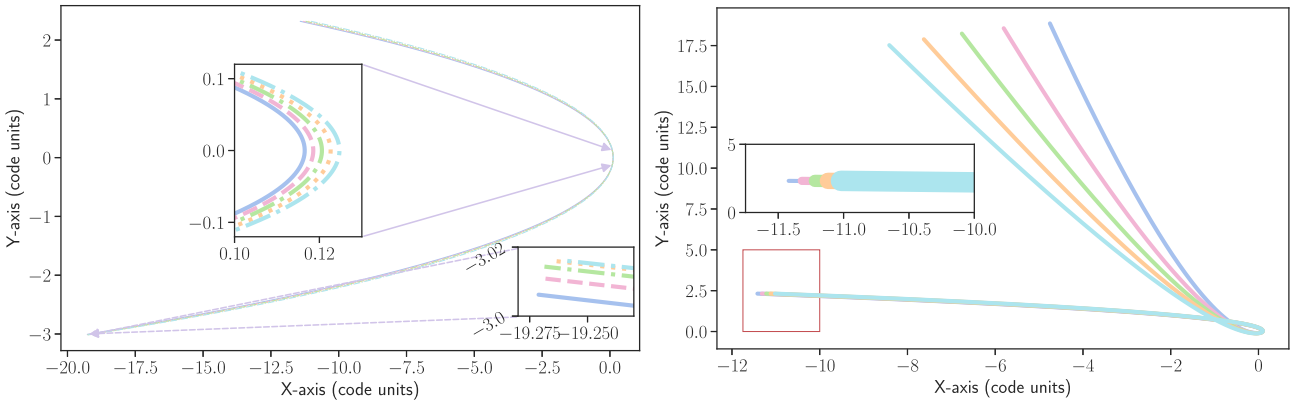

Figure 16. Trajectories in the *XY* plane of six test particles around a MBH in the Newtonian (left) and relativistic (right) cases. In both panels, we display the evolution of the particles and a zoom-in at the pericentre for the Newtonian case. The relativistic one also includes a zoom-in of the initial trajectories of the particles, which are slightly shifted but are otherwise identical. The MBH is located initially at the origin. The test particles have a mass 10^{-14} times smaller than than of the MBH. The initial penetration factor is set to $\beta = 1.2$ for numerical reasons, since the programme will declare the particles as relativistic mergers for deeper factors.

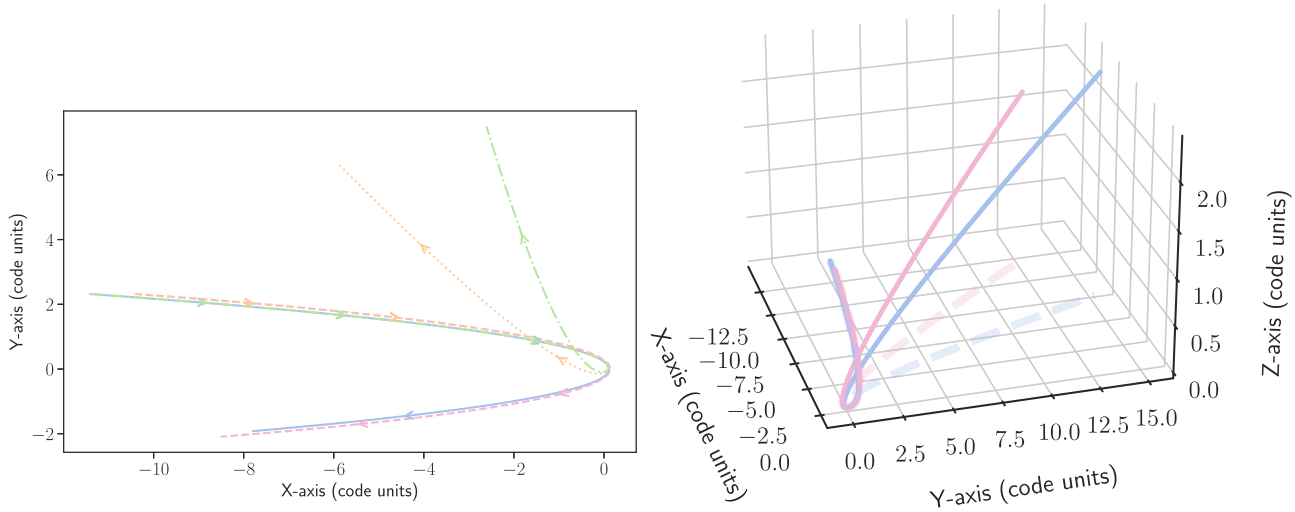

Figure 17. Trajectories in a volume *XYZ* of two test particles around a MBH for the relativistic case without (left) and with spin (right). In the second case, the trajectories leave the initial plane of the orbit and obtain a z component. We display in arrows the sense of the motion of the test particles in the upper, left-hand panel.

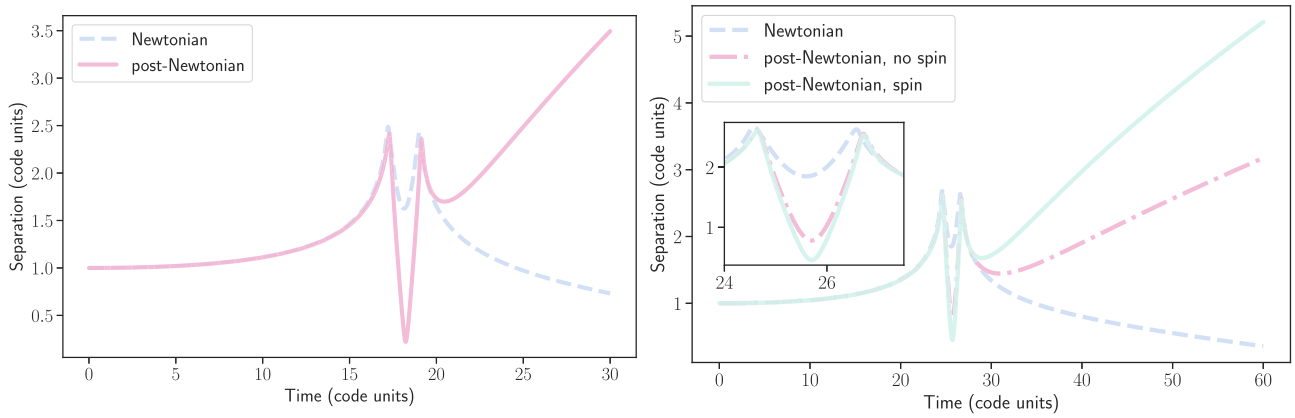

Figure 18. Difference between two particles along their orbit around a MBH in the Newtonian and relativistic case. In the latter, we also display the case with and without spin for the MBH (right-hand panel). We include a zoom-in in the right panel to clearly show the difference at the periapsis passage.

$$\lambda_1 = -\frac{Gm_\bullet}{r^2c^2}\left(1-\frac{2Gm_\bullet}{rc^2}\right)^{-1} + \left[\frac{Gm_\bullet}{c^2r^4}\left(\frac{Gm_\bullet}{c^2}\left[\frac{r}{\left(1-\frac{2Gm_\bullet}{rc^2}\right)^2}-20\right]+8r\right)\right]^{1/2} \tag{19}$$

$$\lambda_2 = -\frac{Gm_\bullet}{r^2c^2}\left(1-\frac{2Gm_\bullet}{rc^2}\right)^{-1} - \left[\frac{Gm_\bullet}{c^2r^4}\left(\frac{Gm_\bullet}{c^2}\left[\frac{r}{\left(1-\frac{2Gm_\bullet}{rc^2}\right)^2}-20\right]+8r\right)\right]^{1/2}, \tag{20}$$

which are always real when $r > R_{\rm Schw}$.

We can derive the values of the two constants by considering the initial conditions. Since the two test particles are part of the dust star, initially the distance between the two is a fixed quantity, which, at most, admits a value of $2R_\odot$ since that is the diameter of the star; also, at time $t = 0$, the change in the distance is zero. I.e. the particles are neither moving away from each other nor closer because the star is considered to be in equilibrium. Therefore,

$$\xi^r(0) \leq 2R_\odot, \left.\frac{\mathrm{d}\xi^r}{\mathrm{d}t}\right|_{(0)} = 0. \tag{21}$$

We therefore have that

$$\xi^r(0) = C_1 + C_2 \leq 2R_\odot, \tag{22}$$

$$\left.\frac{\mathrm{d}\xi^r}{\mathrm{d}t}\right|_{(0)} = \lambda_1 C_1 + \lambda_2 C_2 = 0. \tag{23}$$

From the last equation, we obtain

$$C_1 = \frac{\xi^r(0)}{2}(1-\chi) \tag{24}$$

$$C_2 = \frac{\xi^r(0)}{2}(1+\chi), \tag{25}$$

where we have defined

$$\chi := \frac{r^2Gm_\bullet}{2}\left[Gm_\bullet\left(2c^6r^3+40c^2G^2m_\bullet^2r + (c^2-16)c^4Gm_\bullet r^2 - 32G^3m_\bullet^3\right)\right]^{-1/2}. \tag{26}$$

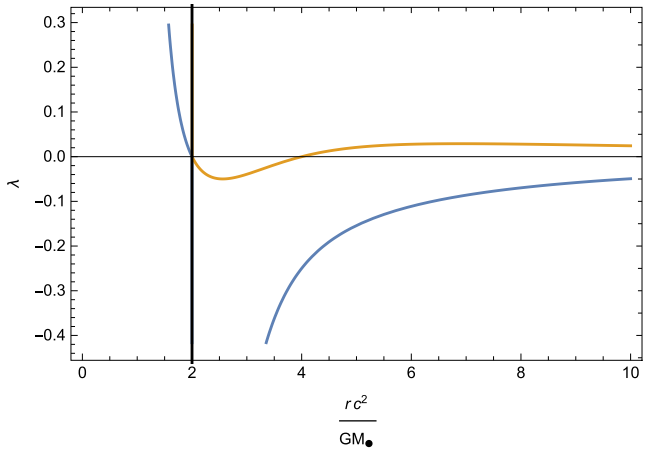

Figure 19. Evolution of the two exponents resulting from the solution of the geodesic deviation equation, λ_1 (blue curve) and λ_2 (orange curve), with respect to the radial distance (normalized by half $R_{\rm Schw}$). The MBH Schwarzschild radius is noted with a black vertical line. Within this radius, both solutions are identical and represented by the same blue curve. We name the region corresponding to the range of values for which both exponents are negative the maximum compression zone.

This quantity drops rapidly as r grows. This means that, far away from the MBH, the two coefficients tend to the same. As a result, both exponential solutions ($e^{\lambda_1 t}$ and $e^{\lambda_2 t}$) are non-zero and neither can be assumed to be very small and negligible.

At this point, in order to examine which of the exponents is more significant, it is useful to examine their behaviour with respect to the radial distance. Notably, one solution (λ_1) is always negative for $r > R_{\rm Schw}$; hence, the corresponding exponential ($e^{\lambda_1 t}$) refers to a shrinking solution for any radial distance of the star from the MBH. The second solution (λ_2), however, alternates sign; it is negative when $R_{\rm Schw} < r < 2R_{\rm Schw}$, and positive when $r > 2R_{\rm Schw}$. As a result, the corresponding exponential solution is shrinking when the particles (i.e. the star) are close to the MBH, and expanding when they are way from it, as we can see in Fig. 19.

As we can see from Fig. 19, the effect of convergence of geodesics is maximized when $R_{\rm Schw} < r < 2R_{\rm Schw}$, which we dub the maximum compression zone, because both exponents are negative. However, not all test particles will necessarily fall this close to the MBH. The star will generally have a larger penetration factor. For larger radii, one of the two exponents is not negative anymore (the orange curve, λ_2). In order to understand how the distance between the two test particles will evolve in the case in which we are outside of the maximum compression zone, we observe that in equation (8.2), the coefficient of $\mathrm{d}\xi^r/\mathrm{d}t$ is larger for small r, but drops faster than the coefficient of ξ^r, so that it can be safely ignored outside the maximum compression zone. In this regime therefore the geodesic deviation equation becomes

$$\frac{\mathrm{d}^2\tilde{\xi}^r}{\mathrm{d}t^2} + \left[\left(\frac{2Gm_\bullet}{r^2c^2}\right)^2 - \frac{2G\,m_\bullet}{r^3}\left(1-\frac{2Gm_\bullet}{rc^2}\right)\right]\xi^{\rm r} = 0. \tag{27}$$

The solution is again of the form

$$\tilde{\xi}^r = C_1 \mathrm{e}^{\lambda_1 t} + C_2 \mathrm{e}^{\lambda_2 t}, \tag{28}$$

where the exponents can be determined by the characteristic equation to be

$$\lambda_1 = \frac{1}{r^2}\sqrt{2Gm_\bullet r\left(1-\frac{4Gm_\bullet}{rc^2}\right)}$$
$$\lambda_2 = -\frac{1}{r^2}\sqrt{2Gm_\bullet r\left(1-\frac{4Gm_\bullet}{rc^2}\right)}, \tag{29}$$

and

$$C_1 = C_2 = \frac{\xi^r(0)}{2} \tag{30}$$

are the constants (determined by the same initial conditions, as before). These solutions contains two exponential functions; one shrinking and the other one expanding at the same pace. Obviously, for large times (i.e. large r), the growing exponential will dominate and the geodesics will deviate, as we saw in the numerical calculations, e.g. Fig. 17. This was indeed expected since we are not taking into account the hydrodynamics of the problem because we do not need it for the short time-scales of interest. Therefore, this solution, although mathematically correct, is physically irrelevant.

In more interesting (shorter) time-scales, as the star (and hence the dust particles) is getting closer to the periapsis distance of the MBH, both terms will contribute. One exponent will tend to bring closer together the test particles and the other one to increase their distance. To ponder how these two concurring exponents affect the global evolution of the two geodesics, we introduce a 'half-life' time-scale, a characteristic time-scale for an exponent to dominate over the other,

$$t_{\rm HL} = \frac{1}{\lambda_1} = \frac{1}{|\lambda_2|}. \tag{31}$$

This time-scale is calculated to be

$$t_{\rm HL} = r^2\left[2Gm_\bullet r\left(1-\frac{4Gm_\bullet}{r}c^2\right)\right]^{-1/2} \propto r^{3/2}, \tag{32}$$

which means that the time-scale of the growing exponential to dominate the shrinking one grows with $r^{3/2}$. As a result, the solutions can be expressed as

$$\tilde{\xi}^r \sim \frac{\xi^r(0)}{2}\left[\exp\left(\frac{t}{r^{3/2}}\right) + \exp\left(-\frac{t}{r^{3/2}}\right)\right]. \tag{33}$$

Of course, as the particles travel in a parabolic orbit, they initially come close to the MBH (r drops over time until they reach periapsis), and then they go away from it (r grows over time after they leave periapsis). This effect is captured by the initial growth of the 'half-life' time, which is followed by a rapid shrinkage, as illustrated in Fig. 20. As a result, as the particles come close to periapsis, the geodesics converge (the closer they come to the MBH, the smaller the distance between them). At later times, and as we discussed previously, the dust particles will start to deviate in their geodesics, but this effect is not physical. What matters is the effect on shorter time-scales as the star is approaching periapsis, because the convergence of geodesics, when generalised to a full star, imply the building up of a core that will withstand the tidal forces of the process and survive the disruption, as we find in the hydrodynamical simulations. We note that, although in our configuration the star initially is in the plane of the orbit, in a more general case in which θ and $\dot{\theta}$ do not vanish, the result remains qualitatively the same, as we are working from the point of view of a comoving observer.

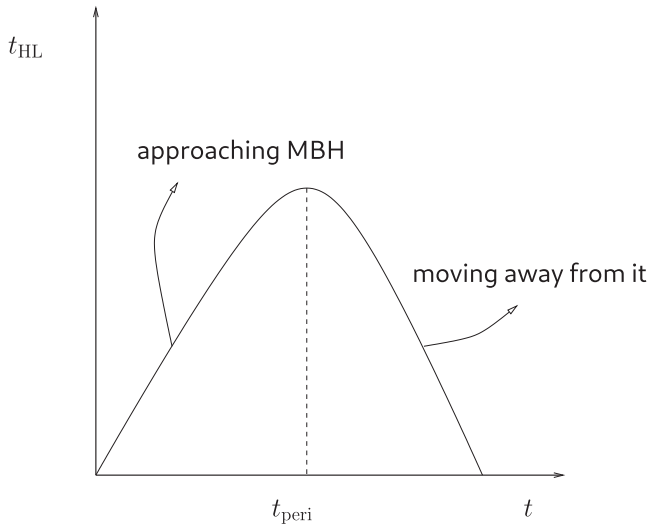

Figure 20. Schematic illustration of the 'half-life' time-scale, which grows as the star approaches the MBH, reaching a maximum at pericentre. Later, it drops as the star moves away from it. During the first half, the geodesics converge, leading to the buildup of a central core. The closer the star comes to the MBH the stronger this effect. During the second half, as the star is moving away from the MBH, the geodesics diverge, but this regime is not relevant, as explained in the main body of the text.

9 CONCLUSIONS

In this work, we have addressed the problem of TDEs being less luminous than theoretically expected in the accretion disc model. We run a set of Newtonian SPH simulations of an unbound star of one solar mass and a MBH of mass $10^6\,{\rm M}_\odot$ with penetration parameters ranging from 1.64 to 12.05. We re-do the simulations with exactly the same β parameters and initial conditions, but taking into account relativistic (post-Newtonian) corrections. For this, we consider two different sets of simulations: one that only includes the first correction to periapsis shift in the equations of motion and another that additionally takes into account the spin-orbit coupling correction up to next-to-lowest order. For β values starting at $\beta \gtrapprox 2.25$, all relativistic simulations feature a surviving core of the original star. The Newtonian simulations, however, do not. Only the lowest value of $\beta = 1.64$ in the Newtonian case displays a core that does not last long enough to be bound to the original star. As a consequence, the fallback rates are lower in the corresponding relativistic cases, and hence the luminosity is also lower. The deeper the TDE, the bigger the difference in luminosity between the Newtonian and relativistic simulations. The effect of the spin only plays an important role, as expected, for extremely deep penetration factors. This was also noted by the work of Gafton & Rosswog (2019), who find that precession leads to debris configurations that are absent in the Newtonian cases.

Moreover, in the relativistic cases, the energy distribution is more spread out, so that in each specific energy bin there is less matter. Hence, the fall back rate in every time-step is lower; $\mathrm{d}M/\mathrm{d}t$ is closely related to $\mathrm{d}M/\mathrm{d}E$, with E the specific energy relative to the MBH. This can be seen in, e.g. fig. 3 of Evans & Kochanek (1989) and the work of Ryu et al. (2020a, 2020b), which show that TDEs in the relativistic case have an energy distribution with significant wings, as well as fig. 2 of Ryu et al. (2020c, 2020d) for a full disruption. If E is wider, $\mathrm{d}M/\mathrm{d}E$ will be smaller and, thus, $\mathrm{d}M/\mathrm{d}t$ as well.

We also study the opening of the debris in the relativistic case and find that the spin allows it to leave the initial plane of the orbit. The probability of debris from the gas, which has been confined within the plane, colliding with itself or with parts of the star is high. As the debris follows different ballistic trajectories, the different fractions of the star, both on their way to the apocentre and those that have been left behind, may eventually interact, producing energetic bursts.

The analysis has been primarily addressed with SPH simulations, complemented by a dynamical numerical toy model of test particles. For this, we examine the behaviour of geodesics in the context of test particles of a star approaching a black hole, neglecting the role of hydrodynamics, i.e. a dust star. We evaluate the distance between the geodesics of these test particles with a precise dynamical code, ARChain, which features post-Newtonian corrections as the ones we have implemented in the hydrodynamical code, since the scheme is also based on the work of Kupi et al. (2006). This exercise is useful because we can neglect the role of the hydrodynamics in the regime in which the relativistic corrections are important, i.e. during the periapsis passage. The idea is that the time-scale in which hydrodynamics plays a role is longer than the time-scale during which relativity plays a role. Hence, the results are to be interpreted only during the periapsis passage. The trajectories of the particles represent the tidal deformation experienced by the star as it approaches the black hole. We find that this distance decreases in the relativistic case, in particular in the one with spin, as the star gets closer to the black hole, indicating that the star is being stretched by the tidal forces. This stretching effect is a key factor in the tidal disruption of the star. It is important to note that we find that this distance remains finite, indicating that the star does not get completely disrupted but retains a core. Finally, we investigate these results analytically using the relativistic equation of geodesic deviation and confirm the numerical findings, i.e. different parts of the star experience a compression during periapsis passage, which is responsible for the building up of a denser core that survives the disruption, contrary to the Newtonian calculations.

Our results suggest that in Nature TDEs must have deeper penetration parameters than previously thought to explain the observations. These orbits naturally lead to the consequence of a reduced observed luminosity regardless of the accretion disc, simply due to the fact that relativity allows a part of the star to survive the disruption.

ACKNOWLEDGEMENTS

The initial idea of this work was presented as a talk at the Alájar meeting in 2013[1] and later as an invited talk at the workshop 'TDE17: Piercing the sphere of influence'[2], which took place in Cambridge. PAS thanks Enrico Ramírez-Ruiz, Pablo Laguna, Zoltan Haiman, Julian Krolik, Nick Stone, Sterl Phinney, Ramesh Narayan, and Stephan Rosswog for comments during the workshop, as well as Julian Krolik for pointing out the publications by him and his collaborators. The simulations performed with ARChain were possible thanks to Seppo Mikkola, who provided us with a copy of his code.

DATA AVAILABILITY

Any data used in this analysis are available on reasonable request from the first author.

[1] Workshop Alájar 2013.
[2] Workshop Cambridge 2017.

REFERENCES

Amaro-Seoane P., 2018, Living Rev. Relativ., 21, 4
Amaro-Seoane P., Miller M. C., Kennedy G. F., 2012, MNRAS, 425, 2401
Arcavi I. et al., 2014, ApJ, 793, 38
Baumgardt H., Amaro-Seoane P., Schödel R., 2018, A&A, 609, A28
Blanchet L., Iyer B. R., 2003, Class. Quant. Grav., 20, 755
Brem P., Amaro-Seoane P., Spurzem R., 2013a, MNRAS, 434, 2999
Brem P., Amaro-Seoane P., Spurzem R., 2013b, MNRAS, 434, 2999
Brenneman L., 2013, Measuring the Angular Momentum of Supermassive Black Holes. Springer
Carter B., Luminet J. P., 1982, Nature, 296, 211
Carter B., Luminet J. P., 1983, A&A, 121, 97
Chandrasekhar S., 1942, Physical Sciences Data. University of Chicago press, Chicago, Ill
Chandrasekhar S., 1998, The Mathematical Theory of Black Holes. Oxford University Press
Chornock R. et al., 2014, ApJ, 780, 44
Evans C. R., Kochanek C. S., 1989, ApJ, 346, L13
Faye G., Blanchet L., Buonanno A., 2006, Phys. Rev. D, 74, 104033
Frank J., Rees M. J., 1976, MNRAS, 176, 633
Freitag M., Benz W., 2002, A&A, 394, 345
Freitag M., Benz W., 2005, MNRAS, 358, 1133
Fulbright M. S., Benz W., Davies M. B., 1995, ApJ, 440, 254
Gafton E., Rosswog S., 2019, MNRAS, 487, 4790
Gallego-Cano E., Schödel R., Dong H., Nogueras-Lara F., Gallego-Calvente A. T., Amaro-Seoane P., Baumgardt H., 2018, A&A, 609, A26
Gezari S., Halpern J. P., Komossa S., Grupe D., Leighly K. M., 2003, ApJ, 592, 42
Gezari S. et al., 2012, Nature, 485, 217
Guillochon J., Ramirez-Ruiz E., 2013, ApJ, 767, 25
Hills J. G., 1975, Nature, 254, 295
Holoien T. W. S. et al., 2014, MNRAS, 445, 3263
Ivanov P. B., Chernyakova M. A., 2006, A&A, 448, 843
Kesden M., 2012, Phys. Rev. D, 85, 024037
Khabibullin I., Sazonov S., Sunyaev R., 2014, MNRAS, 437, 327
Krolik J., Piran T., Ryu T., 2020, ApJ, 904, 68
Kupi G., Amaro-Seoane P., Spurzem R., 2006, MNRAS, 371, L45
Lai D., Rasio F. A., Shapiro S. L., 1993, ApJ, 412, 593
Li L.-X., Narayan R., Menou K., 2002, ApJ, 576, 753
Magorrian J., Tremaine S., 1999, MNRAS, 309, 447
Mikkola S., Merritt D., 2006, MNRAS, 372, 219
Mikkola S., Merritt D., 2008, AJ, 135, 2398
Miles P. R., Coughlin E. R., Nixon C. J., 2020, ApJ, 899, 36
Murphy B. W., Cohn H. N., Durisen R. H., 1991, ApJ, 370, 60
Nandra K. et al., 2013, preprint (arXiv:1306.2307)
Noble S. C., Krolik J. H., Hawley J. F., 2009, ApJ, 692, 411
Peters P. C., 1964, Phys. Rev., 136, 1224
Piran T., Svirski G., Krolik J., Cheng R. M., Shiokawa H., 2015, ApJ, 806, 164
Price D. J., 2007, PASA, 24, 159
Rasio F. A., 2000, Prog. Theor. Phys. Supp., 138, 609
Rees M. J., 1988a, Nature, 333, 523
Rees M. J., 1988b, Nature, 333, 523
Reynolds C. S., 2014, Space Sci. Rev., 183, 277
Ryu T., Krolik J., Piran T., Noble S. C., 2020a, ApJ, 904, id.98
Ryu T., Krolik J., Piran T., Noble S. C., 2020b, ApJ, 904, 99
Ryu T., Krolik J., Piran T., Noble S. C., 2020c, ApJ, 904, 100
Ryu T., Krolik J., Piran T., Noble S. C., 2020d, ApJ, 904, 101
Schödel R., Gallego-Cano E., Dong H., Nogueras-Lara F., Gallego-Calvente A. T., Amaro-Seoane P., Baumgardt H., 2018, A&A, 609, A27
Servin J., Kesden M., 2017, Phys. Rev. D, 95, 083001
Springel V., 2005, MNRAS, 364, 1105
Stone N. C., Vasiliev E., Kesden M., Rossi E. M., Perets H. B., Amaro-Seoane P., 2020, Space Sci. Rev., 216, 35
Syer D., Ulmer A., 1999, MNRAS, 306, 35
Tagoshi H., Ohashi A., Owen B. J., 2001, Phys. Rev. D, 63, 044006
Tejeda E., Gafton E., Rosswog S., Miller J. C., 2017, MNRAS, 469, 4483
van Velzen S., Farrar G. R., 2014, ApJ, 792, 53
van Velzen S. et al., 2020, ApJ, 908, 4
Wang J., Merritt D., 2004, ApJ, 600, 149
Wheeler J., 1971, in O'Connell D. J. K., ed., Study Week on Nuclei of Galaxies. American Elsevier, Amsterdam: North Holland, and New York, p. 539
Zhou Z. Q., Liu F. K., Komossa S., Cao R., Ho L. C., Chen X., Li S., 2020, ApJ, 907, 77

This paper has been typeset from a TEX/LATEX file prepared by the author.